

Low-cycle fatigue of AlSi10Mg processed by laser powder bed fusion using recycled powder: Experimental results and machine learning-assisted lifetime prediction

Michal Bartošák^{a,*}, Michal Jambor^b, Jiří Halamka^a, Lukáš Pelikán^a, Ondřej Stránský^a, Eliška Galčíková^a, Michal Slaný^a, Jakub Horváth^a, Šimon Petrášek^a, Ivo Šulák^{b,**}

^aFaculty of Mechanical Engineering, Czech Technical University in Prague, Technická 4, 166 07 Praha 6, Czech Republic

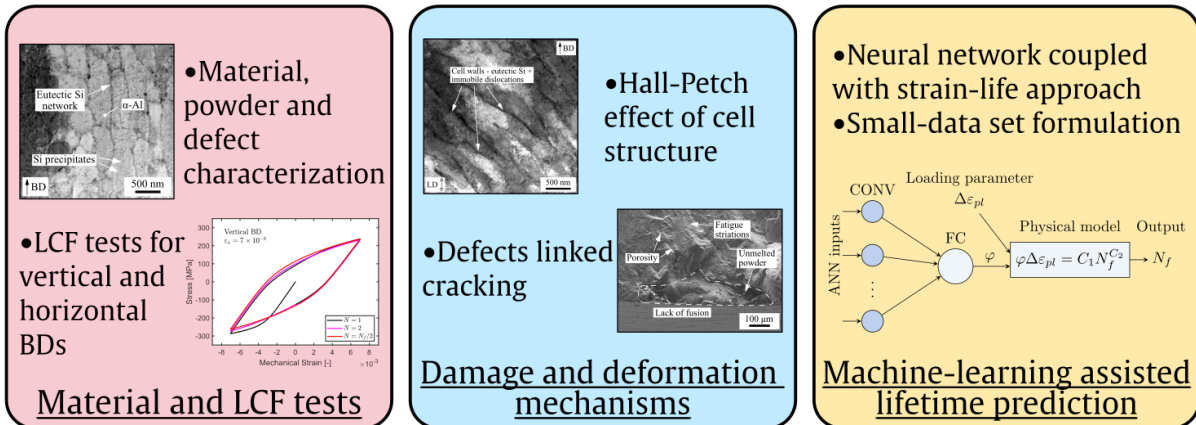
^bInstitute of Physics of Materials, Czech Academy of Sciences, Žitkova 22, 616 00 Brno, Czech Republic

Abstract

In this article, strain-controlled Low-Cycle Fatigue (LCF) tests were performed on laser powder bed fusion-processed AlSi10Mg using recycled powder. The use of recycled powder led to an increased oxygen content, resulting in more pores in the microstructure. The LCF tests covered various strain amplitudes under tension-compression for both horizontally and vertically built specimens. After the initial softening, the cyclic response stabilized, with the Hall-Petch effect identified as the main strengthening mechanism due to the eutectic cell walls, regardless of build direction. Investigations into the damage mechanisms revealed deposition defects as the main factor influencing transgranular crack initiation and propagation. Horizontally built specimens exhibited shorter fatigue lifetimes due to a higher number of deposition defects caused by their positions on the build platform. In order to account for the damaging effects of these deposition-related defects on fatigue lifetime, a physics-informed neural network was combined with a strain-life approach to predict the lifetime of AlSi10Mg. The predicted data showed a good correlation with the experimental results.

Graphical abstract

Low-cycle fatigue of AlSi10Mg processed by LPBF using recycled powder



Keywords:

*michal.bartosak@fs.cvut.cz

**sulak@ipm.cz

Highlights:

- Low-cycle fatigue tests were conducted on LPBF AlSi10Mg using recycled powder.
- Deposition defects from platform position matter more than powder recycling.
- Transgranular cracking linked through the defects is the predominant mode of failure.
- The Hall-Petch effect of cell structure is the main strengthening factor.
- The strain-life approach is combined with neural networks to predict lifetime.

1. Introduction

Additive Manufacturing (AM) technologies are integral to Industry 4.0, offering reduced manufacturing steps and minimal processing waste [1, 2, 3]. Rapidly evolving, AM is increasingly vital for product innovation, especially in high-tech industries, allowing for the fabrication of complex components with designs which would be impossible using traditional manufacturing tools. Laser Powder Bed Fusion (LPBF), also known as selective laser melting or direct metal laser sintering, is the most commonly used AM technique, allowing for the fabrication of components with tailorable ultra-fine, metastable, and gradient microstructures formed by rapid solidification [4, 5, 6, 7, 8, 9]. In the LPBF process, a focused energy source selectively sinters or melts layers of the powder bed [1, 4, 5, 10]. Since only a fraction of the metal powder is consumed during LPBF, the powder outside the processing area can be recycled and reused. However, the high temperature of the LPBF and the interaction between the virgin powder and the laser may induce microstructural and morphological changes in the virgin powder near the parts being built [11, 12]. As the powder reuse cycle increases, many of the original properties of the metallic powder are expected to change [13, 14, 15]. At present, there is a limited understating of the microstructural and mechanical properties of AM parts via LPBF using recycled powder. Therefore, it is particularly important to investigate the microstructure, damage and deformation mechanisms, and mechanical properties of products fabricated using the LPBF process with recycled powder.

AlSi10Mg aluminium alloy fabricated via LPBF has received increasing attention due to its lightweight, high specific strength, and excellent corrosion resistance, making it suitable for applications in the aerospace, automotive, and marine industries [16, 17, 18, 19, 20, 21, 22]. The properties of LPBF AlSi10Mg significantly depend on the post-processing heat treatments performed [18, 23, 24], with most studies focusing on the as-built or stress-relieved conditions [25, 26, 27, 14]. The very high cooling rates during the LPBF process typically result in a fine and unique microstructure of LPBF AlSi10Mg, characterized by hierarchical features such as grain and cell structures, nanoscale Si-based precipitates, and pre-existing dislocation networks [28, 29]. It has been shown that LPBF AlSi10Mg parts possess a higher strength than conventionally fabricated alloy counterparts produced through casting or powder metallurgy [8, 28, 30, 31]. Several investigators have studied the deformation mechanisms of LPBF AlSi10Mg, predominantly under monotonic loading conditions. Wu et al. [28] conducted in-situ compression tests in a Transmission

Electron Microscope (TEM) and discovered that cell boundaries, sub-cell boundaries, and particles within the cells restrict dislocation movement during the deformation of as-built AlSi10Mg. The high strength of as-built LPBF AlSi10Mg was attributed to its very fine cell-like structure, where fine Si precipitates and eutectic Si boundaries impede dislocation motion during plastic deformation [28]. Chen et al. [26] identified Orowan looping as the primary strengthening mechanism, leading to high strain-hardening rates in the LPBF AlSi10Mg alloy. Both Si precipitates and eutectic Si were found to hinder dislocation motion and act as hardening mechanisms during loading at high strain rates of LPBF AlSi10Mg [21]. Furthermore, Hadadzadeh [14] investigated the strengthening mechanisms of both virgin and recycled AlSi10Mg powders in the as-built state under tensile loading. The strengthening of the recycled LPBF AlSi10Mg was attributed to the Orowan mechanism (due to the existence of Si precipitates), the Hall-Petch effect (due to the eutectic cell walls), and dislocation hardening (due to a pre-existing dislocation network) [14]. While there were small differences in the levels of individual strengthening mechanisms, the overall strength of the virgin and recycled LPBF AlSi10Mg, resulting from the combined total contributions, was comparable. Although there have been multiple studies on deformation mechanisms under monotonic loading, there is a lack of understanding of the deformation and strengthening mechanisms of LPBF AlSi10Mg under cyclic loading.

The build parameters and heat treatment are widely known to significantly affect the fatigue properties of the final product [32, 33, 34]. The AM process typically results in various deposition defects, such as gas porosity or Lack of Fusion (LoF) defects [25, 35, 36, 37, 38], which have a detrimental effect on the observed lifetime in both Low-Cycle Fatigue (LCF) and High-Cycle Fatigue (HCF) loading regimes [25, 35, 36, 39, 40, 41]. Defect size has been identified as the principal cause of variability in the fatigue resistance of LPBF AlSi10Mg [42]. Therefore, defect features are typically determined using techniques such as 3D X-ray Computed Tomography (CT) [25, 39, 35, 43]. Furthermore, it has been shown that the build orientation may have an effect on the uniaxial fatigue strength of LPBF AlSi10Mg [44, 25]. Horizontally built specimens typically have a higher fatigue lifetime than vertically built specimens, especially in the HCF loading regime [44]. The decreased fatigue resistance for vertically built specimens is attributed to a different orientation of deposition defects (mainly LOF defects), which have a larger projected area in the plane perpendicular to the loading axis, leading to a lower lifetime [45, 25]. In contrast, the effect of build orientation on the observed lifetime was not significant during strain-controlled LCF tests [46]. Xu et al. [47] investigated the effects of building directions and melt pool boundaries on the fatigue performance and crack propagation of LPBF AlSi10Mg. It was shown that the melt pool boundaries exhibited strain concentration, which subsequently affected fatigue crack propagation. Furthermore, it was ascertained by in-situ X-ray imaging that the cracking behavior of LPBF AlSi10Mg tends to be dominated by large LoF type defects randomly located near the free surface of specimens [48]. There have been a limited number of studies regarding the fatigue performance of LPBF AlSi10Mg using recycled powder [49, 50]. It was reported that up to eight cycles of powder reuse have a negligible effect on the tensile properties of AlSi10Mg, while the fatigue strength decreased by up to 10% [49]. While several studies have mainly focused on the HCF fatigue behaviour of LPBF AlSi10Mg, there is a lack of understanding of the damage mechanisms under strain-controlled LCF loading. Additionally, the effect of using recycled powder on the predominant damage mechanisms during LCF loading is yet to be investigated.

The deposition defects introduced during the LPBF process are a dominant factor

influencing the initiation and propagation of fatigue cracks [32, 33, 34, 51]. Therefore, these defects should be incorporated into the fatigue lifetime prediction techniques designed for AM alloys. Traditionally, the size of the defects is represented by the effective area projected perpendicular to the loading direction, following the Murakami approach, which employs the square root of the area method [52, 45]. Using this approach, lifetime is typically determined using a fracture mechanics-based concept, where the effective area is used to calculate the stress intensity [53, 54, 55, 42]. Most often, lifetime is calculated based on the analysis of the single largest defect. While this approach may be suitable for the HCF domain, where typically a single crack initiation spot appears, it may be inappropriate for the LCF regime, where multiple crack initiations typically occur [56]. In the LCF regime, numerical finite-element modeling coupled with a statistical approach has been used to investigate the damaging effects of deposition defects by explicitly modeling the defects within a representative material volume [56, 57, 58, 59, 60]. Although this approach is highly accurate, the computational expenses may make it unsuitable for the design of AM components. To overcome these challenges, machine learning models [61, 62, 63, 64, 65] appear to be the most promising for incorporating defect features into fatigue lifetime predictions. While Bao et al. [61] used a support vector machine to incorporate the effects of defects and to predict the HCF lifetime of LPBF-processed Ti6Al4V alloy, Artificial Neural Networks (ANNs) have been used more frequently to predict the fatigue lifetime [62, 63, 64, 65]. For example, Li et al. [66] used ANNs to predict the HCF lifetime of Ti-6Al-4V alloy, and Zhan and Li [67] predicted the fatigue lifetime of AM 316L stainless steel by directly incorporating the process parameters into an ANN-based model. However, the disadvantages of using ANNs include the difficulty of interpretation and the lack of extrapolation capability beyond the training dataset. In order to enhance extrapolation capability, physics-informed neural networks have been proposed [68, 69, 70, 71, 72, 73]. While several machine learning methods have been suggested for predicting the lifetime of AM metals, there is limited understanding of their capabilities or the potential to couple machine learning-based methods with classical strain-life lifetime prediction techniques.

In this study, the mechanical behaviour of AlSi10Mg processed by LPBF using recycled powder under LCF loading conditions is investigated. Newly reported experimental results focus on LPBF-processed AlSi10Mg with recycled powder. Light Microscopy (LM) and Scanning Electron Microscopy (SEM) are employed to investigate damage mechanisms and microstructure, while X-ray CT is used to analyze the morphology and distribution of deposition defects within the specimen volumes. Deformation mechanisms and nanoscale microstructure are further examined using Transmission Electron Microscopy (TEM). Additionally, a machine learning approach is combined with a strain-life approach to predict the LCF lifetime of LPBF-processed AlSi10Mg using a small dataset. This article is structured as follows: Section 2 describes the materials and methods. Section 3 presents the results and discussion, covering material and defect characterization, a study of damage and deformation mechanisms, cyclic mechanical behaviour, and lifetime evaluation and prediction under LCF loading. Finally, conclusions are drawn in Section 4.

2. Materials and methods

This section provides an overview of the methods used for performing experiments, lifetime prediction, and the microstructural observations on LPBF-processed AlSi10Mg using recycled powder. Subsection 2.1 first details the nominal chemical composition and provides further information on the LPBF process and the heat treatment of the

Table 1: The nominal chemical composition of AlSi10Mg aluminium alloy virgin powder in wt. % (indicative values).

Si	Mg	Fe	Mn	Ti	Cu	Zn	C	Ni	Pb	Sn	Al
9.0–11.0	0.2–0.45	<0.55	<0.45	<0.15	<0.10	<0.10	<0.05	<0.05	<0.05	<0.05	Bal.

investigated material. Next, Subsection 2.2 describes the experimental procedures for the strain-controlled LCF tests conducted on plain cylindrical specimens. The methods for microstructural observations and X-ray CT scanning are outlined in Subsection 2.3. Finally, Subsection 2.4 briefly describes the artificial neural networks used to incorporate the effects of the damaging defects on fatigue lifetime within the strain-life approach.

2.1. Investigated material

The material under investigation is AlSi10Mg aluminium alloy processed by LPBF using recycled powder, with the process carried out on a Concept Laser M2 machine under a nitrogen atmosphere. The virgin AlSi10Mg powder, supplied by Concept Laser, a GE Additive company, under the commercial name CL 31AL, was used in this study. The nominal chemical composition of the virgin powder is provided in Tab. 1. The AlSi10Mg powder underwent 13 recycling cycles. Each cycle involves transporting the powder from the container to the printer. Any powder not exposed during a deposition process is transferred to the next container. The next step is the gradual dosing of the powder into the sieving station, where it is sieved under a nitrogen atmosphere using an 80-micrometer sieve. Initially, there was 40 kg of powder. Since the amount of powder decreases with each deposition process, it was replenished twice: 20 kg after 6 cycles and an additional 10 kg after 10 cycles. In this study, specimens were AM using both vertical and horizontal build directions. For the vertical build direction, the build direction z was aligned with the axis of the specimen. Conversely, for the horizontal build direction, the axis of the specimen lay in the xy plane and was perpendicular to the build direction.

The Concept Laser skin-core deposition strategy was employed for the LPBF of the specimens. The default layer thickness was 25 μm . The contour is deposited first, followed by the skin. Both the contour and skin are exposed in every layer, maintaining a layer thickness of 25 μm . The deposition strategy for the skin is zigzag (laser power: 200 W, scanning speed: 1250 mm/s, laser spot size: 100 μm). Subsequently, the core is deposited. The core is exposed in every second layer, resulting in a layer height of 50 μm . The core deposition strategy is a chessboard pattern (laser power: 370 W, scanning speed: 1400 mm/s, laser spot size: 190 μm), where individual square areas measuring 8×8 mm are exposed in random order with a zigzag deposition strategy to ensure even heat distribution across the exposed area. The location of the LPBF-processed specimens on the build plate is shown in Fig. 1(b) with respect to the recoater movement direction. Additionally, the specimens used for performing the LCF tests are labelled with numbers. After deposition, the specimens underwent stress relief heat treatment, involving heating to 240°C over 1 hour, holding at this temperature for 6 hours, then cooling in the furnace to 100°C. Afterwards, the specimens were cooled in ambient conditions.

Following the heat treatment, the specimens were machined, with the contour and part of the skin of each specimen removed. The geometry of the specimens is illustrated in Fig. 1(c).

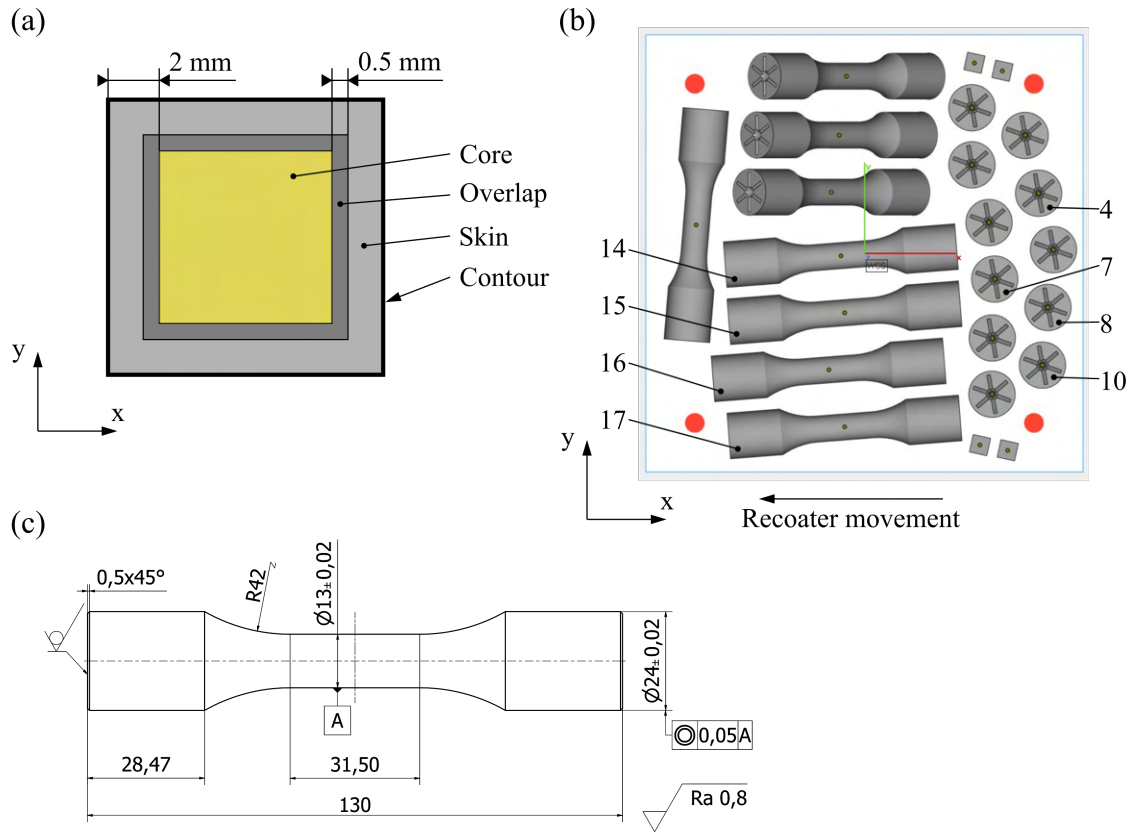


Figure 1: Scheme of the utilized skin-core deposition strategy for LPBF-processed AlSi10Mg using recycled powder (a). View of the LPBF-processed specimens on the build plate (b). The geometry of the specimen used for the strain-controlled LCF tests, with dimensions provided in millimetres (c).

2.2. Low-cycle fatigue tests

The strain-controlled LCF tests were conducted on cylindrical plain specimens with a gauge diameter of 13 mm, Fig. 1(c). The parallel length of the specimen was 32 mm, and the gauge length was 25 mm. These experiments were conducted under ambient conditions on a servo-hydraulic axial-torsional testing machine e.g. [74, 75, 76]. The mechanical strain was controlled by an extensometer with a gauge length of 25 mm. The LCF tests were performed on both horizontally and vertically built specimens with a constant mechanical strain rate of 1×10^{-3} /s (triangular loading waveform) for four different mechanical strain amplitudes, ε_a , between 4×10^{-3} and 7×10^{-3} . Four specimens were used to conduct the LCF tests for the horizontal build direction, and another four were used for the vertical build direction. Finally, the end-life criterion, which is used here to determine the number of cycles to a failure, N_f , is defined as a 5% decrease in the maximum stress of the cycle under the tangent line through the saturated part of the evolution of the maximum axial stress with cycles.

2.3. Microstructural observations and X-ray computed tomography

For the purpose of conducting metallographic observation, sections of LPBF-processed AlSi10Mg were prepared in two distinct orientations: one parallel to the build direction and the other perpendicular to it. Following the cutting and pressing of the samples into a conductive compression mounting compound, they were ground using P280-P4000 grit and then polished with colloidal SiO₂. Grinding and polishing were conducted on an automatic grinding and polishing system, the LECO GPX 300. To observe the microstructure, the specimens were etched at room temperature using Keller's solution (1% hydrofluoric acid, 1.5% hydrochloric acid, 2.5% nitric acid, and 95% distilled water). The microstructure and fracture surfaces were observed using a Neophot 32 metallographic LM and a JEOL JSM-7600F SEM equipped with an Energy-Dispersive X-ray Spectroscopy (EDS) detector. Furthermore, the microstructure at the nanoscale of the LPBF-processed AlSi10Mg alloy was observed by utilizing TEM using a Thermo Scientific TalosTM F200i TEM, which operates at 200 kV and is equipped with an EDS detector. TEM micrographs were acquired in scanning mode (STEM) at a resolution of 2048×2048 pixels with a point resolution of 0.2 nm. The thin lamellae for TEM scrutiny of the initial microstructure after heat treatment were produced using the Focused Ion Beam (FIB) lift-out procedure in a dual-beam SEM, the Tescan LYRA 3 XMU, operating at 30 kV. Details of the FIB-TEM lift-out procedure are provided elsewhere [77]. Post-mortem microstructural analysis of specimens after cyclic straining was conducted on thin foils cut from the gauge length of the fatigued specimens. Before observation, the foils were dimpled to a thickness of approximately 80 μ m and further thinned using an Ar-ion milling system (PIPS II, Gatan Inc.) with a beam energy of 4 kV and incident angles of 10°. Additionally, particle size distributions of both the AlSi10Mg virgin and recycled powders were analysed using the Microtrac CAMSIZER X2 system for dynamic image analysis.

Furthermore, prior to LCF testing, selected specimens were scanned using X-ray CT. A Zeiss Metrotom 1500 CT machine, equipped with a 225 kV X-ray source, was used. The machine was set up to 180 kV and 136 μ A with a 0.25 mm copper prefilter. The positioning of the specimen allowed for the entire gauge section to be scanned at once. However, only a cylindrical section of 32 mm in length was used for the evaluation. The measurement parameters resulted in a magnification of 9.09, a natural voxel size of 22 μ m, and a 24 μ m spot size. A total of 1250 continuous projections were collected with a 1000 ms exposure time. The obtained data were reconstructed using Metrotom OS 3.6.2.19227 and further

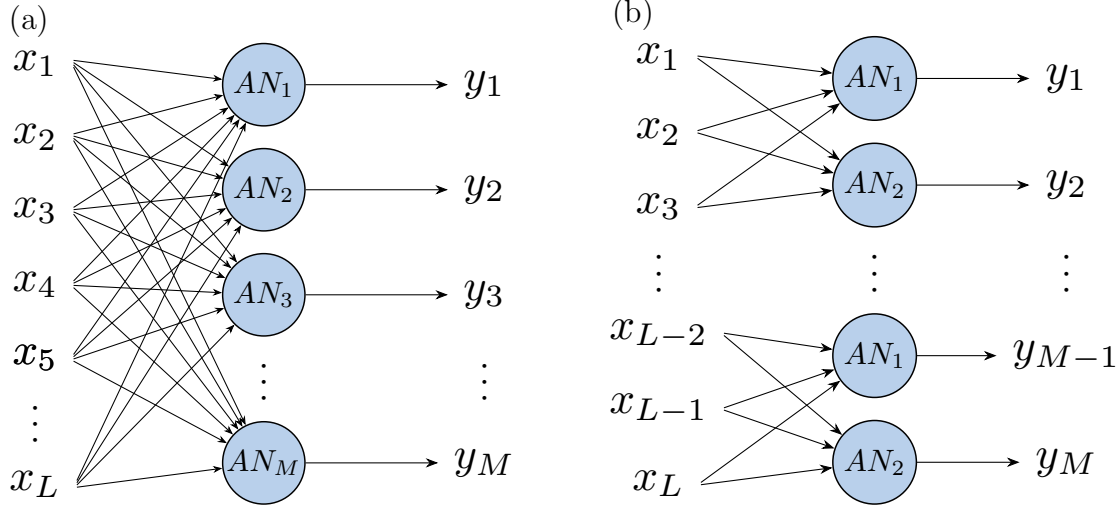


Figure 2: Fully connected layer (a) and convolutional layer (b).

evaluated in VG Studio Max 3.2.2 software. The porosity analysis was performed using the proprietary VGEasyPore algorithm, where detected defects with a probability greater than 1.3 and larger than 15 voxels were considered relevant.

2.4. Artificial neural networks

The main components of Artificial Neural Networks (ANNs) are the Artificial Neurons (ANs). Each neuron provides the mathematical expression to obtain the output value y from the input vector \vec{x} as follows:

$$y = g \left(\sum_{i=1}^N w_i x_i + b \right), \quad (1)$$

where b represents the bias, \vec{w} is the vector of weights, and $g(\dots)$ denotes the activation function, which introduces non-linearity. The ANN is defined by the connections between network inputs, multiple ANs, and network outputs. Initially, the weights and biases of all neurons are randomly initialized and then optimized. This optimization process aims to align the computed outputs, based on given inputs, as closely as possible with the desired targets. Furthermore, two types of layers are used in this study: the Fully Connected (FC) layer and the Convolutional (CONV) layer. The FC layer is defined by the parallel use of multiple ANs, where each neuron connects to the entire input vector, Fig. 2a. In contrast, the CONV layer employs a convolution kernel that computes outputs by sliding across the input vector. Fig. 2b depicts a CONV layer with a kernel consisting of two neurons and a filter size of three inputs. In Fig. 2, L represents the number of inputs, while M denotes the number of outputs. In this work, the stride, which represents the distance by which the kernel slides to compute the next outputs, will be consistently equal to the filter size.

3. Results and discussion

This section presents both experimental and numerical results from Low-Cycle Fatigue (LCF) tests on LPBF-processed AlSi10Mg aluminium alloy. Subsection 3.1 first covers the material characterization before LCF loading, including analyses of deposition defects

and comparisons between virgin and recycled powder. The cyclic mechanical behaviour is examined in Subsection 3.2, while the primary damage and deformation mechanisms are investigated in Subsections 3.3 and 3.4. Cyclic stress-strain and fatigue-life curves are analyzed in Subsection 3.5. Lastly, Subsection 3.6 combines machine learning with a strain-life approach in order to predict LCF lifetime.

3.1. Material and defects characterization

The morphology and size of both AlSi10Mg virgin and recycled powder were analyzed using SEM, as shown in Figs. 3(a) and (b), respectively. It can be observed that the powder recycling revealed no significant change of powder morphology, which remained nearly spherical with occasional irregular and elongated particles which are typical for both virgin and recycled powder. Furthermore, the EDS mapping of oxygen is shown in the bottom left corners of both Figs. 3(a) and (b). EDS analysis revealed an oxidized surface on the recycled powder, leading to higher oxygen content in the build produced from the recycled powder. It is known that the oxygen content gradually increases as the reuse of powder increases in metal AM [78, 79]. This increase in oxygen content occurs because the stored reused powder can absorb oxygen from handling and from the storage environment, while reactive powders may oxidise during use [80, 81]. Furthermore, the relative and cumulative distribution curves of particle diameter are shown for both virgin and recycled powder in Fig. 4(c). The 10th (D_{10}), 50th (D_{50} , i.e. average particle size) and 90th (D_{90}) percentiles of powder particle diameter are 17.17 μm , 34.38 μm , and 54.53 μm for the virgin powder, and 16.98 μm , 34.19 μm , and 53.58 μm for the recycled powder. It can be observed that the particle size distributions are almost identical for virgin and recycled powders. Therefore, it can be concluded that with the utilized recycling strategy, powder recycling has no significant effect on powder particle size changes. Similarly, Maamoun et al. [12] reported that powder recycling has no significant effects on the powder particle size distribution. In contrast, Del Re et al. [49] found that the powder particle diameter changed to lower values with an increasing number of powder reuses. However, they used a different batch of AlSi10Mg powder and utilized a different sieve size to those used in this study. Additionally, it was shown that the major changes occur only during the first two powder reuses [49].

Figs. 3(c)–(f) show light microscope images of the microstructure for LPBF-processed AlSi10Mg using virgin and recycled powder. Along the build direction, both virgin and recycled powder feedstocks exhibit a typical fish-scale morphology with clearly visible melt pools with a half-cylindrical shape, Figs. 3(c) and (d). Perpendicular to the build direction, interwoven scan tracks corresponding to the build strategy can be observed for both types of powder feedstock, Figs. 3(e) and (f). Pores are evident in both the virgin and recycled powder samples, appearing spherical and likely gas-induced. Occasionally, irregularly shaped pores, known as LoF defects, are also observed, Figs. 3(e). LoF defects may occur due to insufficient energy during the melting process or spatter ejection [82, 50]. Comparing the micrographs of LPBF-processed AlSi10Mg using virgin and recycled powder, a higher number of pores is observed in the recycled powder feedstock. Additionally, larger pores occasionally appear in the LPBF-processed AlSi10Mg using recycled powder, Figs. 3(f). Leung et al. [80] studied how powder oxidation affects molten pool dynamics and defect formation in AM. Oxides in the powder are entrained into the molten pool, altering the Marangoni convection from an inward centrifugal to an outward centripetal flow [80]. Their findings confirm that excessive oxygen in the powder feedstock can lead to defects by serving as a nucleation site for pores and subsequently stabilising these pores

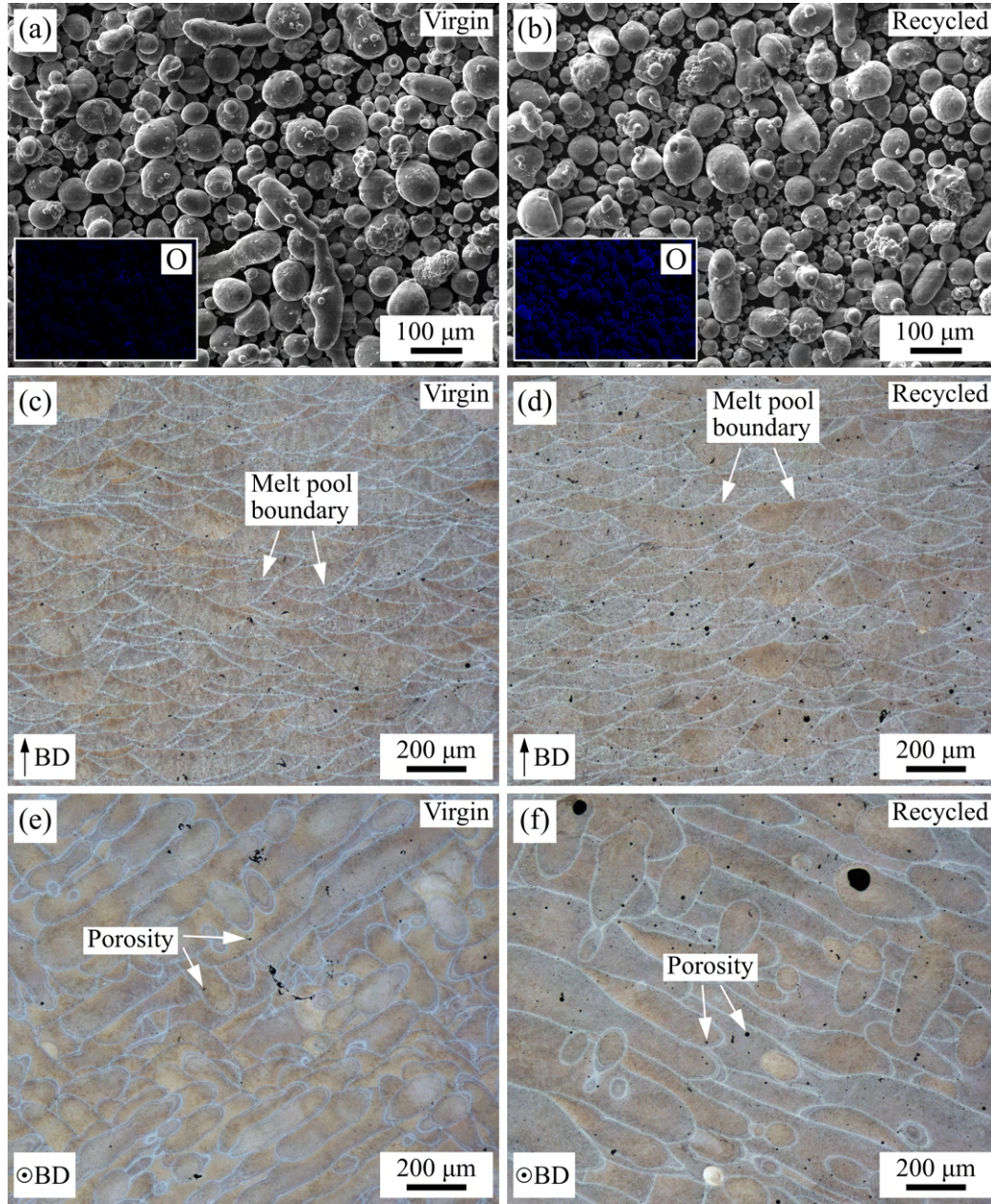


Figure 3: SEM images of AlSi10Mg virgin (a) and recycled (b) powder including oxygen EDS analysis (bottom left corners). Light microscope micrographs of the initial microstructure after heat treatment of LPBF-processed AlSi10Mg using virgin powder: plane parallel to the Build Direction (BD) (c) and plane perpendicular to BD (e); for LPBF-processed AlSi10Mg using virgin powder: plane parallel to BD (d) and plane perpendicular to BD (f). The use of recycled powder results in higher porosity due to elevated oxygen content compared to the virgin powder.

[80]. Therefore, the increased presence of pores observed in the microstructure of LPBF-processed AlSi10Mg using recycled powder (Figs. 3(d) and (f)) in this study is attributed to the elevated oxygen content of the recycled powder feedstock. It is known that an increased number of defects decreases fatigue resistance [35]. Thus, it is suggested that the use of recycled powder would slightly decrease the fatigue performance of AlSi10Mg compared to virgin powder, with a more pronounced effect under HCF loading than under the LCF loading regime.

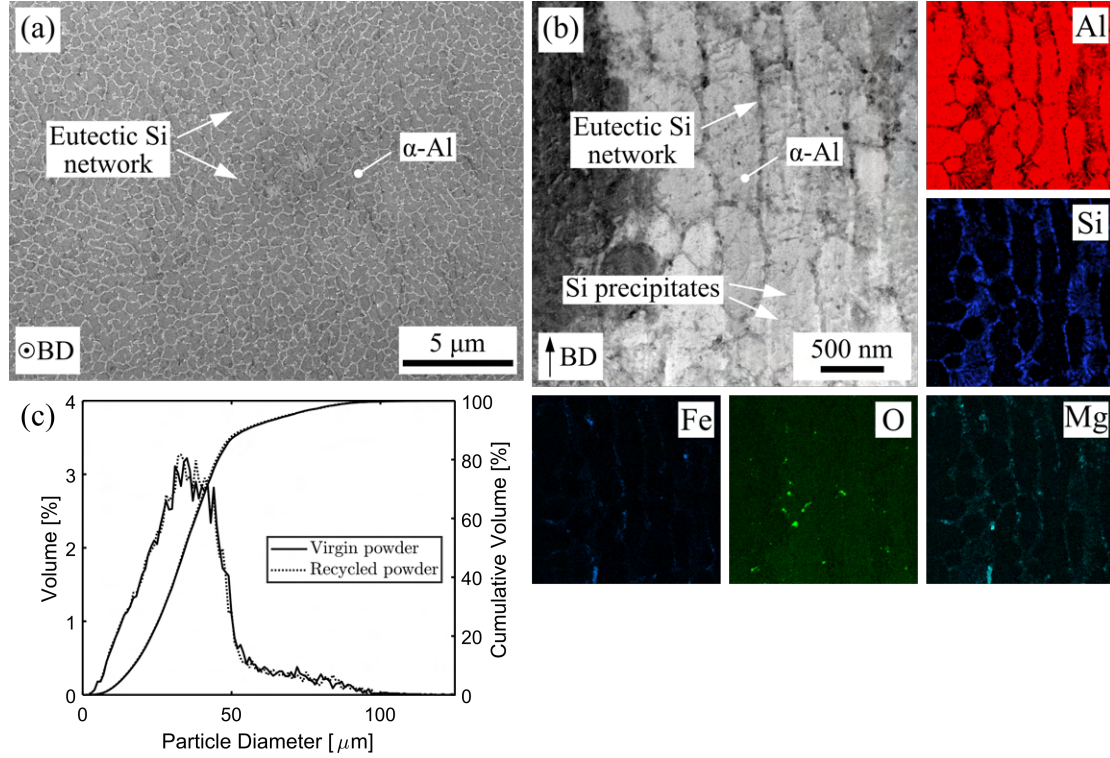


Figure 4: SEM micrograph of the initial microstructure after heat treatment of LPBF-processed AlSi10Mg using recycled powder shows the solidification cells of α -Al separated by eutectic Si network (plane perpendicular to Build Direction (BD)) (a). BF STEM micrograph of the initial microstructure after heat treatment for LPBF-processed AlSi10Mg using virgin powder (b) (plane parallel to BD), including the associated EDS mapping, provides a more detailed view of eutectic Si network and Si-based precipitates. Relative and cumulative distribution curves of particle diameter for virgin (solid lines) and recycled (dotted lines) powders are nearly identical (c).

The SEM image of the microstructure of LPBF-processed AlSi10Mg using recycled powder, perpendicular to the build direction, is shown in Fig. 4(a). The BrightField Scanning Transmission Electron Microscopy (BF STEM) micrograph is presented in Fig. 4(b), along with the elemental distribution of Al, Si, Mg, Fe and O in the associated EDS mapping images. LPBF-processed AlSi10Mg exhibits a typical ultra-fine microstructure formed by rapid solidification [83]. The cells, consisting of a supersaturated α -Al solid solution, are separated by a continuous network of intercellular eutectic Si, as shown in Fig. 4(a) [28, 84]. The size of these cells ranges from about 300 to 500 nm, and they appear elongated along the build direction, Fig. 4(b). Referring to the EDS elemental maps of Fe and Mg, various intermetallic phases formed at the cell boundaries, Fig. 4(b) [14]. Inside Al-rich cells, thin needle-like Si precipitates have formed (indicated by white arrows in Fig. 4(b)). It is suggested that due to the multiple recycling of the powder, Mg-based oxides have formed due to an increased oxygen content, as observed in the EDS

maps [14]. Except for the formation of Mg-based oxides, the microstructure in Fig. 4 appears similar to that of LPBF-processed AlSi10Mg using virgin powder and undergoing similar heat treatment [28, 84, 85].

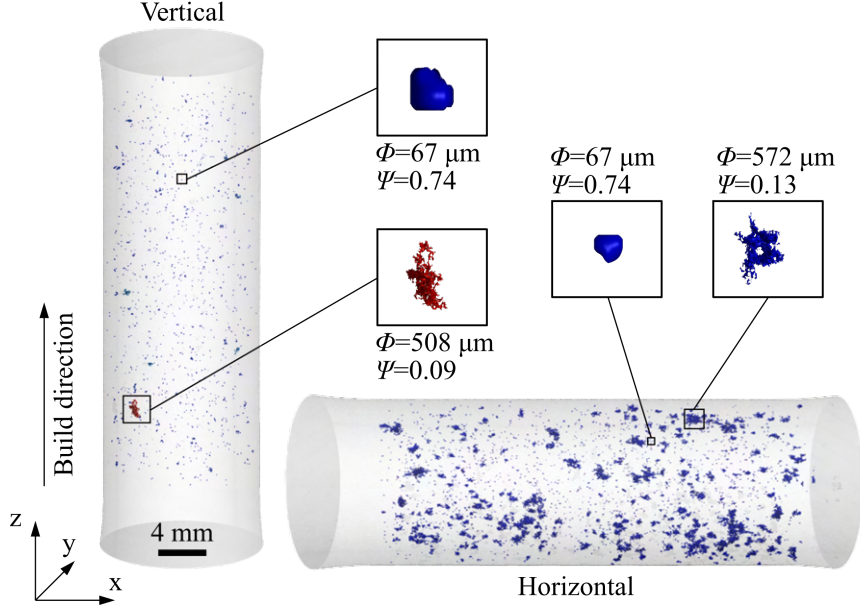


Figure 5: 3D renderings of defects in horizontally and vertically built specimens subsequently subjected to LCF loading with $\varepsilon_a = 6 \times 10^{-3}$ (specimens No. 10 and 14). Typical defect types, such as pores and LoF, are shown in greater detail with selected features highlighted.

Representative 3D volumes of defects within the gauge volume of the vertically and horizontally built specimens (specimens No. 10 and 14 in Fig. 1(b)) are shown in Fig. 5. It should be noted that the results were similar to those of other vertically and horizontally built specimens. It is evident that LPBF-processed AlSi10Mg contains numerous defects of various shapes and sizes, uniformly distributed throughout the volume. Both the vertically and horizontally built specimens exhibited pores. In the vertical build direction, LoF defects were observed only occasionally. In contrast, horizontally built specimens frequently contained LoF defects, as illustrated in Fig. 5. Furthermore, in order to quantify the size and shape of the deposition defects, the effective diameter, Φ , and the sphericity, Ψ [25, 43], are introduced. The effective diameter, Φ , is defined as the diameter of an equivalent sphere with the same volume as the defect, Eq. 2. Sphericity, Ψ , is defined in Eq. 3 as the ratio of the surface area of a sphere (with a volume equal to the defect volume) to the surface area of the defect.

$$\Phi = \sqrt[3]{\frac{6V_d}{\pi}}, \quad (2)$$

$$\Psi = \frac{\pi^{1/3} (6V_d)^{2/3}}{S_d} \quad (3)$$

In Eqs. 2 and 3, V_d denotes the defect volume and S_d represents the defect surface area. Pore defects typically have Ψ values close to 1, indicating a more spherical shape, while LoF defects have Ψ values closer to 0, reflecting their irregular shapes.

The results of the defect analysis are presented in Fig. 6 for the horizontally and vertically built specimens (No. 10 and 14 in Fig. 1(b)) that were subsequently subjected

to LCF loading with $\varepsilon_a = 6 \times 10^{-3}$). The distributions of the sphericity of the individual defects in the vertically and horizontally built specimens are shown in Figs. 6a and 6a, respectively. It can be observed that most defects have a sphericity of around 0.55. For the horizontally built specimen, a second local maximum in the relative frequency around a sphericity value of 0.25 corresponds to LoF defects rather than porosity, Fig. 6b. Relative and cumulative distribution curves of equivalent diameters of defects are plotted for these specimens with horizontal and vertical build directions in Figs. 6c and 6d, respectively. Additionally, the sphericity as a function of the equivalent diameter of defects is shown in Figs. 6e and 6f, for the vertically and horizontally built specimens, respectively. From the distribution curves of equivalent diameter and the sphericity as a function of equivalent diameter, it can be concluded that the majority of defects are small gas pores, as observed in Fig. 3. LoF defects, associated with low sphericity (i.e. irregular morphology) and larger equivalent diameters, are particularly observed in the horizontal build direction, Figs. 6b, 6d and 6f.

It is known that LoF defects have a greater negative effect on the fatigue lifetime compared to pores due to the larger notch effect introduced by their irregular shape [40, 35]. Examining Figs. 3, 5 and 6, it can be deduced that the location of the specimen on the build plate should have a more critical role than powder recycling, which primarily increases the number of gas pores in the microstructure. As specimens are located further from the start position of the recoater, Fig. 1, more LoF defects appeared. This effect can be explained as follows. The recoater movement direction, shown in Fig. 1(b), corresponds to the gas flow direction. Therefore, exhaled particles from the deposition process mix into the powder before the recoater. Additionally, the AlSi10Mg powder particles of varying sizes are randomly distributed within the powder chamber. During the movement of the recoater in the powder chamber, the powder slightly redistributes, with larger particles moving to the top and smaller ones moving to the bottom. As a result, at the start of the recoater's movement in the build chamber, the first specimens (i.e. the vertically built specimens in Fig. 1(b)) may achieve a slightly higher density because they are fabricated using slightly smaller powder particles. This, along with the exhaled particles from the deposition process mixing into the powder, leads to a higher number of LoF defects in the specimens located on the side of the build plate opposite to the recoater's starting position, with the exhalations having a greater effect.

3.2. Cyclic mechanical behaviour

The cyclic evolutions of the minimum and maximum stresses and stress-strain hysteresis loops for varying numbers of loading cycles, N , during the LCF tests that were performed with a constant mechanical strain rate of 1×10^{-3} /and for various strain amplitudes, are plotted in Fig. 7. The cyclic evolutions of the minimum and maximum stresses for the vertically and horizontally built specimens that were cyclically strained are shown in Figs. 7a and 7b, respectively. The LPBF-processed AlSi10Mg aluminium alloy exhibited an initial cyclic softening trend during the first few loading cycles for both build directions, followed by an almost stabilized stress-strain response. It should be noted that there was a mean stress evolution during the cyclic loading of both the vertically and horizontally built specimens. In the case of the vertically built specimens, for the largest applied strain amplitude of 7×10^{-3} the mean stress was about 24 MPa in compression in the first loading cycle, then consistently rose to values of about 13 MPa in compression at mid-life, Fig. 7a. On the other hand, for horizontally built specimens, there was tensile mean stress with consistent evolution towards zero, Fig. 7b. Specifically, for horizontally

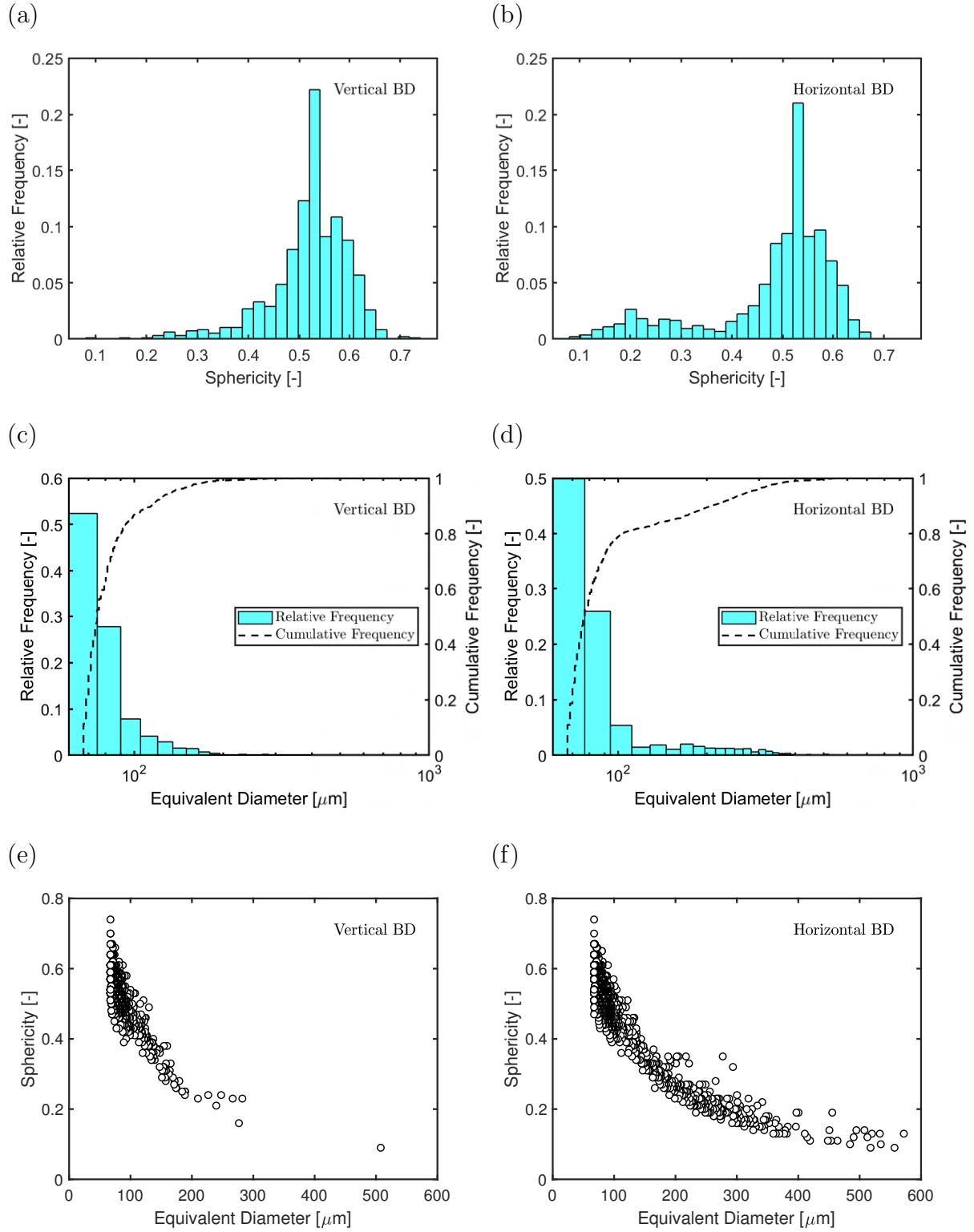


Figure 6: Relative distribution curves of sphericity for vertically (a) and horizontally (b) built specimens. Relative and cumulative distribution curves of defect's equivalent diameter for vertically (c) and horizontally (d) built specimens. Sphericity as a function of equivalent diameter for defects in vertically (e) and horizontally (f) built specimens. The data are presented for specimens subsequently subjected to LCF loading with $\varepsilon_a = 6 \times 10^{-3}$ (specimens No. 10 and 14).

built specimen subjected to mechanical strain amplitude of 7×10^{-3} , there was a low value of tensile mean stress of about 3 MPa in the first loading cycle. Then it consistently rose to values close to zero at mid-life. Similar values and trends in the evolution of mean stresses were observed for other applied strain amplitudes for both build directions. It should be noted that a similar cyclic mechanical behaviour during LCF straining was also observed for LPBF-processed specimens using AlSi10Mg virgin powder that underwent a similar (or none) heat treatment [86, 46]. Therefore, it can be concluded that the applied recycling process of AlSi10Mg powder should not have a significant effect on the cyclic stress-strain response.

Furthermore, the stress-strain hysteresis loops for different numbers of loading cycles from the LCF tests performed with equivalent mechanical strain amplitudes of 4×10^{-3} and 7×10^{-3} , are presented in Figs. 7c, 7d, 7e and 7f. It can be observed that, as expected, the larger the applied strain amplitude, the greater the stress amplitude and plastic strain range. For vertically built specimens, the stress amplitude was around 221 MPa in the first loading and about 202 MPa at mid-life for the LCF test performed with $\varepsilon = 4 \times 10^{-3}$. For $\varepsilon = 7 \times 10^{-3}$, the stress amplitude decreased from 262 MPa in the first loading cycle to about 250 MPa at mid-life. For horizontally built specimens, the magnitudes of stress amplitudes were similar. With cyclic straining at $\varepsilon = 4 \times 10^{-3}$, the stress amplitude was around 220 MPa and about 205 MPa in the first cycle and at mid-life, respectively. Similarly, for $\varepsilon = 7 \times 10^{-3}$, the stress amplitude decreased from around 260 MPa in the initial loading cycle to about 250 MPa at mid-life. As reported above, the build direction affects the mean stresses during LCF loading, while the difference in the stress amplitude values due to build direction is not significant. However, differences can be observed in the shapes of the stress-strain hysteresis loops between the vertical (Figs. 7c and 7e) and horizontal build directions (Figs. 7d and 7f). The yield stress in compression (determined by the 0.2% offset method) during the initial loading cycle was around 272 MPa for the vertically built specimen, whereas it was about 240 MPa in the case of the horizontally built specimen, using data from specimens subjected to LCF loading with $\varepsilon = 7 \times 10^{-3}$. The eutectic Si network is known to impede dislocation motion during plastic deformation [28]. Therefore, these differences in yield stresses may be attributed to the different orientations of the eutectic Si network (Fig. 4) in relation to the direction applied to the loading for horizontal and vertical build directions.

Finally, a summary of the performed LCF tests is provided in Tab. 2, where No. denotes the specimen number corresponding to Fig. 1(b), BD indicates the Build Direction, σ_a and σ_m represent the stress amplitude and mean stress at mid-life ($N_f/2$), respectively, and $\Delta\varepsilon_{pl}$ denotes the plastic strain range, also given at mid-life ($N_f/2$). It can be observed that while the stress amplitudes were similar for both the horizontally and vertically built specimens, the fatigue lifetime was lower in the case of the horizontally built specimens, especially for lower mechanical strain amplitudes, Tab. 2.

3.3. Damage mechanisms

A light microscope and SEM were used to investigate the fracture surfaces of specimens subjected to LCF loading with a mechanical strain amplitude of 6×10^{-3} in order to identify the predominant failure modes for vertical and horizontal build directions. The fracture surfaces of the vertically and horizontally built specimens are presented in Figs. 8 and 9, respectively. An overview of the entire fracture surface of the vertically built specimen from the light microscope is shown in Fig. 8(a), while more detailed SEM views of the selected locations are presented in Figs. 8(b)–(e). Similarly, the entire fracture

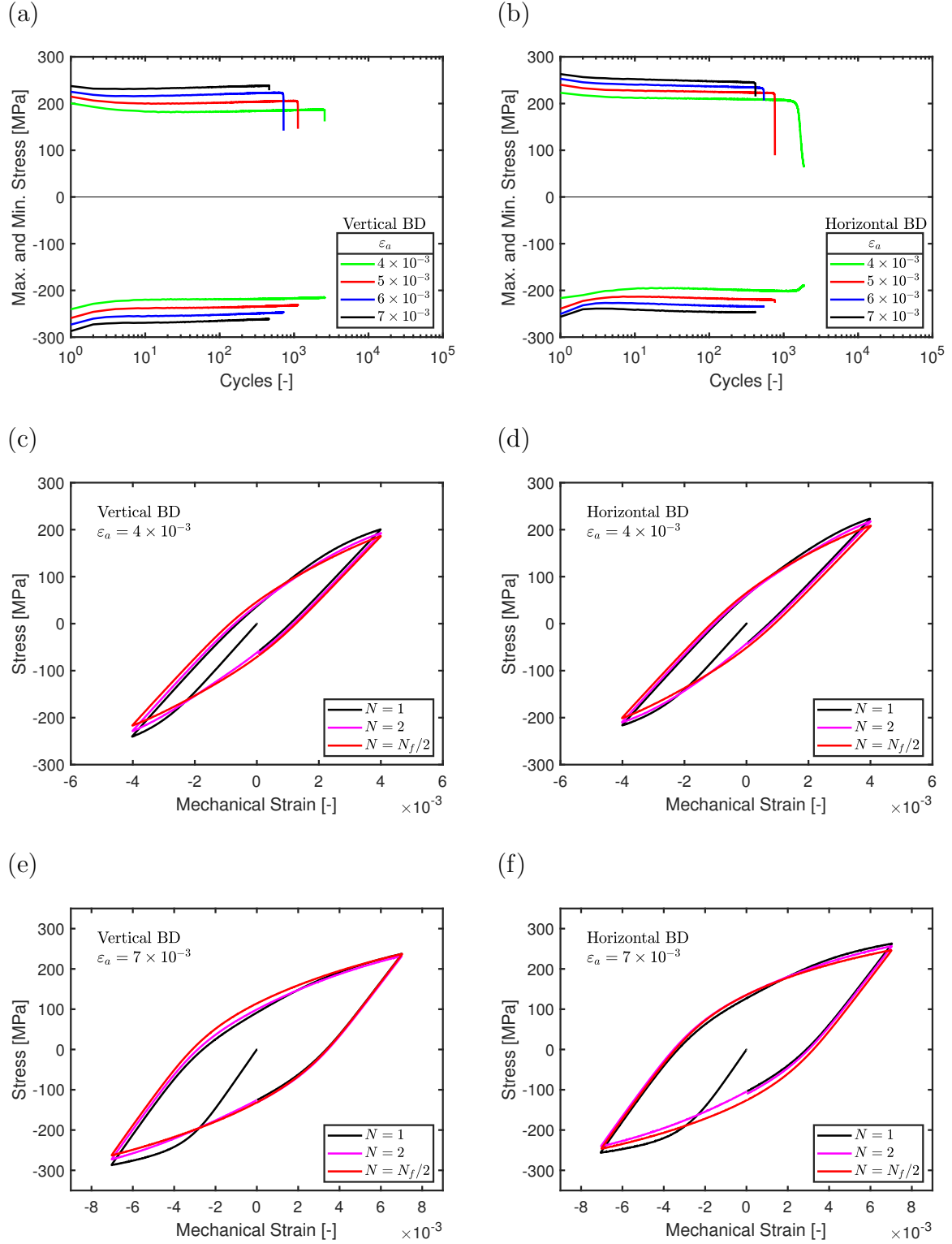


Figure 7: The cyclic evolutions of minimum and maximum stresses in LCF tests performed on vertically (a) and horizontally built specimens (b). Stress-strain hysteresis loops for different numbers of loading cycles in LCF tests performed with $\varepsilon = 4 \times 10^{-3}$ for a vertical (c) and horizontal build direction (d), and for LCF tests performed with $\varepsilon = 7 \times 10^{-3}$ for a vertical (e) and horizontal build direction (f).

Table 2: Summary of the performed LCF tests for LPBF processed AlSi10Mg aluminium alloy using recycled powder.

No.	BD	ε_a [-]	$\sigma_a(N_f/2)$ [MPa]	$\sigma_m(N_f/2)$ [MPa]	$\Delta\varepsilon_{pl}(N_f/2)$ [-]	N_f [-]
7	Vertical	4×10^{-3}	202	-15	2.13×10^{-3}	2577
8	Vertical	5×10^{-3}	219	-15	3.52×10^{-3}	1124
10	Vertical	6×10^{-3}	236	-13	4.98×10^{-3}	719
4	Vertical	7×10^{-3}	250	-13	6.51×10^{-3}	463
17	Horizontal	4×10^{-3}	205	3.6	2.04×10^{-3}	1503
16	Horizontal	5×10^{-3}	221	2.2	3.54×10^{-3}	758
14	Horizontal	6×10^{-3}	234	0.9	5.10×10^{-3}	541
15	Horizontal	7×10^{-3}	246	0.1	6.69×10^{-3}	417

surface of the horizontally built specimen subjected to cyclic straining with $\varepsilon_a = 6 \times 10^{-3}$ is shown in Fig. 9(a), and more detailed views are presented in Figs. 9(b)–(e).

In the case of the vertically built specimen cyclically strained with $\varepsilon_a = 6 \times 10^{-3}$, the fracture surface appeared relatively smooth with a dominant fatigue crack initiation site, as shown in Fig. 8(a). Additionally, multiple deposition defects can be directly observed in Fig. 8(a). A detailed view of the main crack initiation site is provided in Fig. 8(b), revealing that the main crack initiated in the vicinity of a deposition defect, likely a LoF defect. The fatigue crack then propagated transgranularly, as evidenced by the presence of fatigue striations. Occasionally, the secondary cracks also propagated along the boundaries of the melt pools, Fig. 8(b). Pores were frequently observed on the fracture surface, visible in Figs. 8(a), (c) and (d), along with deposition defects such as LoF. A deposition defect containing unmelted powder resulting from the utilized chessboard deposition strategy is shown in Fig. 8(d), which acted as a nucleation site for cleavage fracture. Furthermore, it was observed that further away from the main crack initiation site, cracks propagated more frequently along the boundaries of the melt pools, as seen in Fig. 8(e).

The entire fracture surface of the horizontally built specimen that was subjected to LCF loading with $\varepsilon_a = 6 \times 10^{-3}$ is shown in Fig. 9(a). Similar to the vertically built specimen, there was a dominant fatigue crack initiation site, and multiple deposition defects can be observed directly in Fig. 9(a), with a greater frequency compared to the vertical build direction, consistent with the X-ray CT analysis shown in Fig. 6. Additionally, several secondary crack initiations from deposition defects in the vicinity of the specimen’s free surface were also observed. In contrast to the vertically built specimen, the fracture surface exhibited a cup and cone fracture morphology rather than being smooth. A detailed view of the main crack initiation site is provided in Fig. 9(b), revealing that the main crack initiated from a LoF defect, which was present at the specimen surface and contained unmelted powder. Similarly to the vertically built specimen, fatigue cracks propagated transgranularly, with pores and fatigue striations frequently present in the fracture surface, Figs. 9(b), (c) and (d). It was also shown that further away from the main crack initiation site, cracks propagated more frequently along the boundaries of the melt pools, as seen in Fig. 9(d) and (e). However, the frequency of crack propagation along the boundaries of the melt pools appeared slightly lower than for the vertically built specimen, Fig. 8. The orientation of the melt pools in relation to the loading axis differs for the horizontally built specimens compared to the vertically built ones, which may

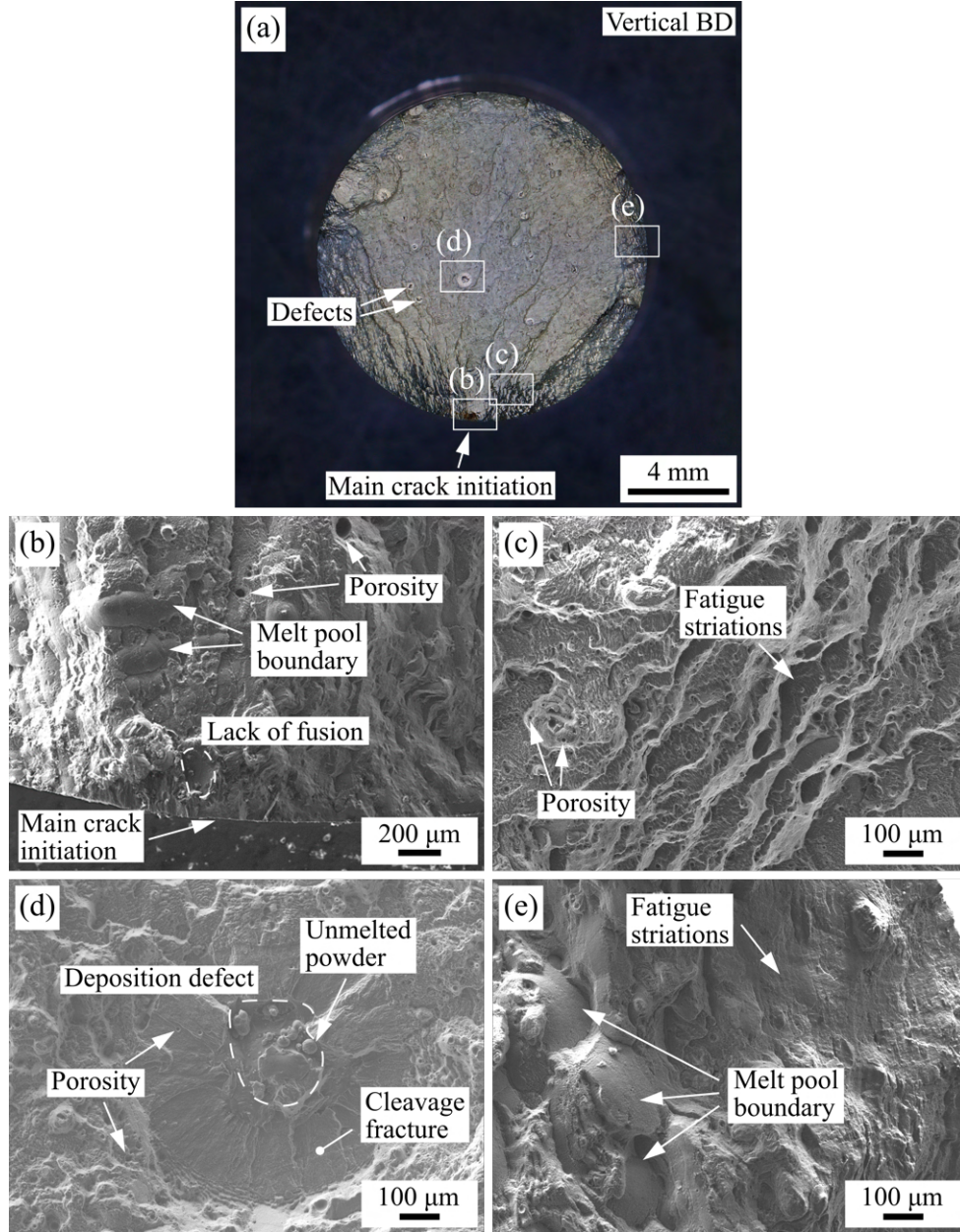


Figure 8: The fracture surface of the vertically built specimen from the performed LCF test with $\varepsilon_a = 6 \times 10^{-3}$. An overview of the entire fracture surface is shown in (a), with a detailed view of the main crack initiation site presented in (b). The transgranular crack propagation is depicted in (c). The fracture morphology around a deposition defect resulting from the deposition strategy is observed in (d), while cracking along the boundaries of melt pools is documented in (e).

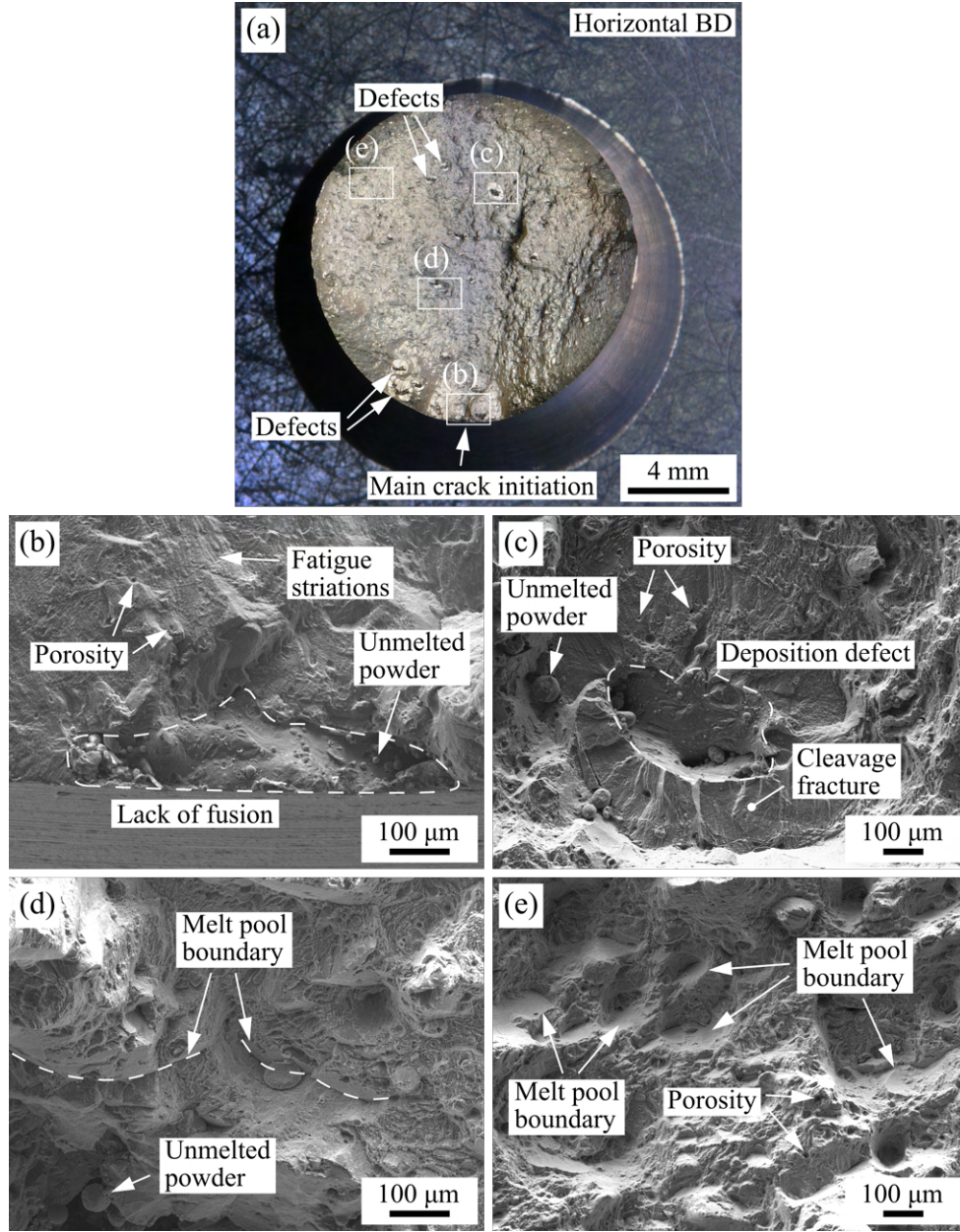


Figure 9: The fracture surface of the horizontally built specimen from the performed LCF test with $\varepsilon_a = 6 \times 10^{-3}$. An overview of the entire fracture surface is shown in (a), with a detailed view of the main crack initiation site presented in (b). The fracture morphology around a deposition defect resulting from the deposition strategy is depicted in (c). The propagation of cracks along the boundaries of melt pools is documented in (d) and (e), with visible deposition defects including LoF and porosity in the fracture surface.

explain the differences in the fracture surface morphology. It should be noted that the cracks occasionally propagated almost vertically on the plane perpendicular to the loading axis, Fig. 9(d). Additionally, a cleavage-like fracture morphology was also observed in the vicinity of the deposition defects resulting from the utilized chessboard deposition strategy, Fig. 9(e).

It should be noted that the results presented in this study correlate with the previously published findings obtained for LPBF-processed AlSi10Mg using virgin powder [42]. Deposition defects near the specimen surface, particularly LoF, typically act as fatigue crack nucleation sites for AM alloys [87, 88, 42]. Similarly to Xu et al. [47], it has been shown that the boundaries of the melt pools influence the fatigue crack propagation, likely due to a strain concentration [47]. Additionally, crack paths are known to typically follow the boundaries of the melt pools under tensile loading [89]. When comparing the obtained results with the literature, it appears there is no significant difference in the predominant damage mechanisms between LPBF-processed AlSi10Mg using virgin and recycled powders. However, the frequency of pores observed in the fracture surfaces may be higher for LPBF-processed AlSi10Mg using recycled powder, as seen in the initial microstructure, Fig. 3. Therefore, the observed fatigue lifetime is expected to be lower for LPBF-processed AlSi10Mg using recycled powder compared to that using virgin powder. This difference is likely to be more pronounced under HCF loading conditions rather than LCF loading.

3.4. Deformation mechanisms

Post-mortem STEM analyses were performed in order to characterize the deformation mechanisms during LCF loading. The microstructures of both the horizontally and vertically built specimens after cyclic straining at a mechanical strain amplitude of 6×10^{-3} are shown in Fig. 10. The BF STEM images show the microstructure of the vertically built specimen in Figs. 10(a) and (c), and the microstructure of the horizontally built specimen in Figs. 10(b) and (d). A more detailed view of the microstructure after cyclic straining is presented using High-Angle Annular Dark-Field (HAADF) STEM imaging for the vertically built specimen in Figs. 11(a) and (c), and for the horizontally built specimen in Figs. 11(b) and (d).

Distinctive differences in the microstructure appearance were observed for both the vertically and horizontally built specimens. The hierarchical nature of the microstructure is evident in both build directions. However, a critical aspect is the orientation of the local heat flow direction with respect to the loading axis of the specimens. In both the examined variants, no localization of plastic deformation was noticed. Dislocation slip took place preferentially within cell interiors. Cell walls, consisting of a network of eutectic Si and immobile dislocations, act as effective barriers to dislocation movement, so slip is mostly restricted within individual cells. The evolutions of maximal and minimal stresses in Fig. 7 show cyclically stable behaviour for the majority of the lifetime for both build directions. This behavior differs from studies performed on similar aluminium alloys with applied post-process heat treatment, which report a pronounced cyclic hardening within the range of applied strain amplitudes [90, 91]. The absence of cyclic hardening can be explained by the lack of microstructural changes introduced by the applied post-process heat treatment. Cyclic plastic deformation in AlSiMg alloys processed by LPBF is mostly determined by the morphology of eutectic Si particles and fine Si-rich particles formed during post-process heat treatment. Since only stress-relieving heat treatment was applied in the present study, the formation of fine strengthening Si-rich particles was suppressed,

removing the source of strengthening due to dislocation accumulation and interactions. A few pinned dislocations can be seen in Fig. 11, however, the overall pinning effect of the present particles is considered negligible. The recycled nature of the powder used in the LPBF process increases the oxygen content in the matrix, resulting in the formation of fine Mg-rich oxide particles. These particles do not seem to have any pronounced effect on the deformation mechanisms during LCF.

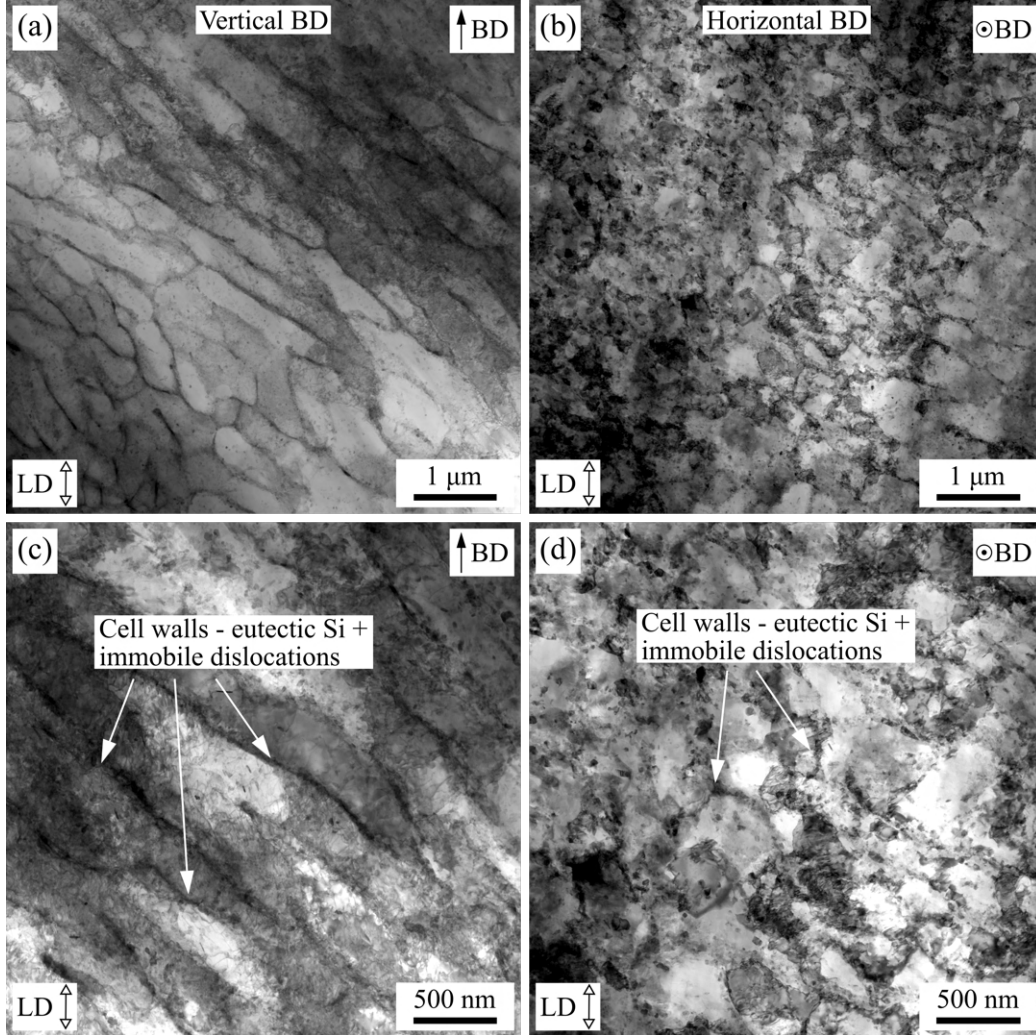


Figure 10: BF STEM images of specimens after cyclic straining with $\varepsilon_a = 6 \times 10^{-3}$. Differences in the microstructure between vertical (a, c) and horizontal (b, d) specimens are clearly visible.

Small differences between the cyclic strength of the horizontally and vertically built specimens (Fig. 7) can be explained by the Hall-Petch effect of cell structure, which is suggested as the main strengthening factor of LPBF-processed AlSi10Mg under LCF loading. Due to the thermal gradients, the effective cell size is larger for vertically built specimens compared to the horizontally built ones, resulting in a smaller mean free path for dislocations for the horizontal specimens (Fig. 11). However, the role of microstructure variations on the overall fatigue properties appears to be insignificant, even though the strain-life curves (see Fig. 12a) show a superior fatigue behaviour of vertically built specimens, particularly for smaller applied strain amplitudes. The presence of LoF deposition defects appears to be a major determining factor for fatigue behaviour, even in the LCF regime.

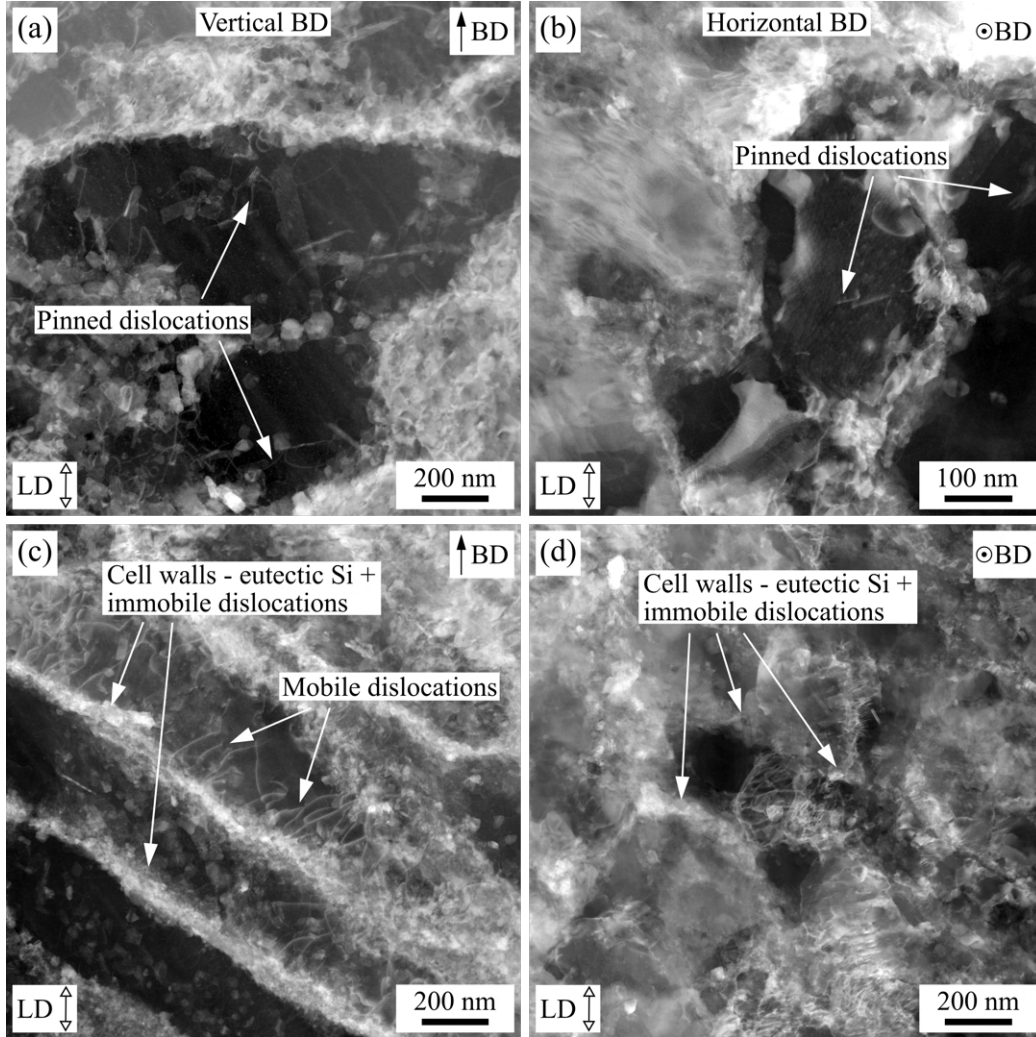


Figure 11: HAADF STEM images of specimens after cyclic straining with $\epsilon_a = 6 \times 10^{-3}$. Intracellular spaces contain a limited amount of precipitation particles, on which are pinned individual dislocations (a, b). In the case of vertically built specimens, cell interiors also contain visible mobile dislocations (c), while the cell interiors within horizontal specimens are almost free of dislocations (d).

3.5. Cyclic stress-strain and fatigue-life curves

The strain-life approach, represented in terms of total mechanical strain amplitude, ε_a , versus the number of cycles to failure, N_f , is commonly described by the Manson-Coffin-Basquin model [92, 93, 94], given as follows:

$$\varepsilon_a = \varepsilon_a^e + \varepsilon_a^{pl} = \frac{\sigma'_f}{E} (2N_f)^b + \varepsilon'_f (2N_f)^c, \quad (4)$$

where the total mechanical strain amplitude, ε_a , is decomposed into the elastic part, ε_a^e , and the plastic part, ε_a^{pl} . Here, E denotes the elastic modulus, σ'_f represents the fatigue strength coefficient, ε'_f is the fatigue ductility coefficient, while b and c represent the fatigue strength exponent and the fatigue ductility exponent, respectively. The parameters of the strain-life curve determined for LPBF-processed AlSi10Mg using recycled powder that was cyclically strained under LCF loading conditions are presented in Tab. 3 for both the vertically and horizontally built specimens. The strain life-curves, as described by the Manson-Coffin-Basquin model, are plotted in Fig. 12a. Furthermore, the Cyclic Stress-Strain Curves (CSSCs) determined for the LPBF-processed AlSi10Mg are presented in Fig. 12b for both the vertically and horizontally built specimens. The cyclic relationship between the stress amplitude, σ_a , and the plastic strain amplitude, ε_a^{pl} , is described by the Ramberg-Osgood model [95], as follows:

$$\varepsilon_a^{pl} = \left(\frac{\sigma_a}{K'} \right)^{1/n'}, \quad (5)$$

where K' denotes the cyclic strength coefficient, and n' represents the cyclic strain hardening exponent. Note that the model is applied to the experimental results, σ_a and ε_a^{pl} , obtained at mid-life (i.e. for $N_f/2$). The fitted coefficients, K' and n' , for the vertical and horizontal build directions are given in Tab. 3.

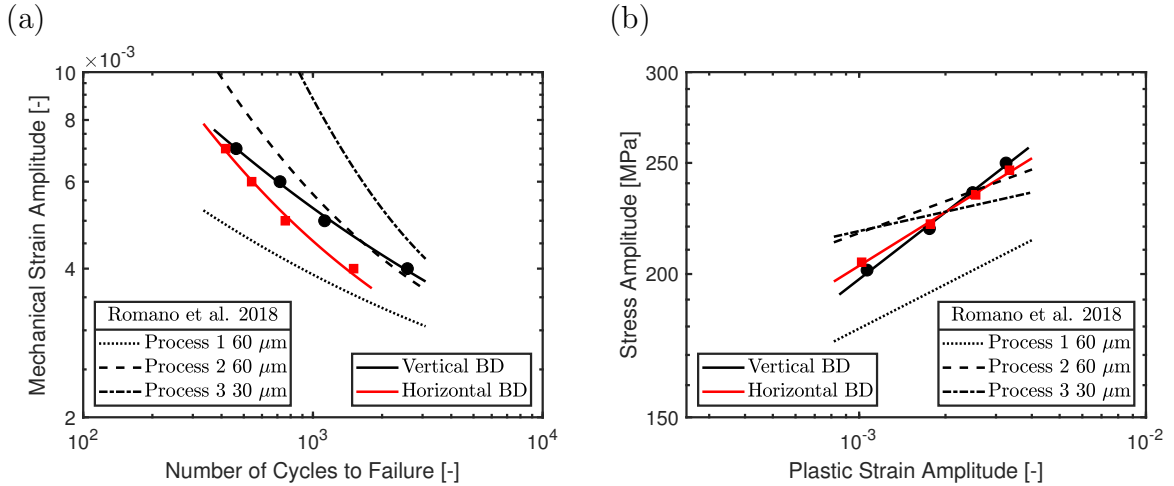


Figure 12: The Manson–Coffin–Basquin strain-life curves of LPBF-processed AlSi10Mg using recycled powder for vertically and horizontally built specimens under LCF loading (a), along with the corresponding cyclic stress–strain curves at mid-life (b). The data are compared with the literature data obtained for LPBF-processed AlSi10Mg using virgin powder and three different build parameters [42], represented by a single regression curve for both horizontally and vertically built specimens for each set of build parameters.

From Fig. 12a, it can be seen that for the largest tested strain amplitude, the observed lifetimes of the vertical and horizontal build directions are almost similar. In contrast,

as the applied strain amplitude decreases, the differences become more significant, with a lower lifetime observed for the horizontal build direction. Wu et al. [25] reported that the lifetime was higher for horizontally built specimens than for vertically built ones in the HCF loading regime. This was attributed to the damaging effects of LoF defects, which have a larger projected area to the plane perpendicular to the tensile axis for vertically built specimens, thereby having a larger damaging effect [45, 25]. Wu et al. [25] used specimens extracted from a block built in a selected spot on the build plate, thus excluding the effect of specimen location on the plate. In our study, different locations of vertically and horizontally built specimens (Fig. 1(c)) led to a different number of deposition defects (Fig. 5), with a higher number of LoF defects observed for the horizontally built specimens. It is suggested that this explains the differences in the observed lifetime. Additionally, greater lifetime reduction for horizontally built specimens compared to vertically built ones confirms that deposition defects have increasingly damaging effects at lower loading amplitudes, as each set of horizontally and vertically built specimens in this study exhibited a similar quantity and morphology of deposition defects. Finally, comparing the CSSCs for horizontal and vertical build directions (Fig. 12b), it can be seen that the CSSCs are almost identical. The only differences between these two build directions in terms of stress-strain response were the initial yield stress value and the differences in mean stress evolution, as described in Section 3.2.

Table 3: Parameters of the cyclic stress-strain curves and strain-life curves of LPBF-processed AlSi10Mg using recycled powder for vertically and horizontally built specimens under LCF loading.

BD	K' [MPa]	n' [—]	σ'_f [MPa]	b [—]	ε'_f [—]	c [—]	E [GPa]
Vertical	756	0.194	695	-1.444	0.303	-0.663	70
Horizontal	596	0.156	738	-0.16	2.384	-0.978	70

The determined cyclic stress-strain curves and strain-life curves of LPBF-processed AlSi10Mg using recycled powder are compared to the literature data of Romano et al. [42] using virgin powder in Figs. 12a and 12b. Romano et al. [42] utilized three different build parameters: Process 1, 2, and 3. The layer thickness was the same at 60 μm for Processes 1 and 2, whereas it was 30 μm for Process 3. Romano et al. [42] represented the fatigue and cyclic stress curves with a single regression curve for both the horizontally and vertically built specimens for each set of build parameters, Fig. 12. It should be noted that the build parameters in the literature are different from those used in this work. However, it can be observed that the data obtained in this study are comparable to the results corresponding to Processes 2 and 3 [42]. The most significant difference is the lower lifetime observed, especially for the horizontally built specimens, which is attributed to a higher frequency of deposition defects compared to the vertically built specimens, Fig. 12a. The powder recycling appears to only increase the number of pores in the microstructure (Figs. 3(c)–(f)). On the other hand, the position of build specimens on the build platform significantly affects the number of LoF defects, which significantly influence fatigue crack initiation. Based on this observation and the literature results indicating that the fatigue lifetime is comparable for vertically and horizontally built specimens [44, 42], it is concluded that the position of specimens on the build plate (Fig. 1(b)) plays a more important role in the LCF lifetime than powder recycling. On the other hand, it is suggested that the increased number of pores in the LPBF-processed AlSi10Mg using recycled powder may significantly affect the HCF results. More rigorous

comparisons of fatigue lifetime using specimens built in the same spot on the build plate and various powder reuse cycles may be the subject of future research. However, the results presented in this study suggest that significant effects of powder recycling on the microstructure should appear for higher powder reuse cycles, specifically above 10.

3.6. Machine learning-assisted lifetime prediction

The lifetime of LPBF-processed AlSi10Mg is significantly influenced by deposition defects. However, no damage model currently exists to account for the effects of multiple defects on fatigue life in a closed form. To address this, a machine learning approach is employed. In this work, physics-informed ANNs are used to integrate defect features and are combined with the strain-life approach represented by the Manson-Coffin relation. The advantage of this approach is its ability to effectively correlate defect populations with LCF lifetime results. The strain-life approach, based on the plastic strain range ($\Delta\varepsilon_{pl}$), is commonly described by the Manson-Coffin fatigue model [93, 94], expressed in its general form as follows:

$$\Delta\varepsilon_{pl} = C_1 N_f^{C_2}, \quad (6)$$

where C_1 and C_2 are material-dependent parameters obtained from experimental results. The difference in fatigue lifetime, N_f , between the vertical and horizontal and build directions is primarily attributed to variations in the population of deposition defects. Therefore, a single fatigue-life curve is assumed for both build directions. In order to account for the damaging effects of deposition defects on LCF lifetime, a damage-based parameter φ is introduced into the Manson-Coffin model as follows:

$$\varphi \Delta\varepsilon_{pl} = C_1 N_f^{C_2}. \quad (7)$$

Here, φ is computed individually for each specimen by a proposed ANN, based on the characteristics of the deposition defects.

The LPBF-processed AlSi10Mg specimens typically exhibited a single main crack initiation site, though secondary cracks were also observed. Therefore, predicting fatigue lifetime based solely on the largest defect is inadequate, as LCF often involves multiple initiation sites and secondary cracks as observed in Subsection 3.3. For these reasons, it is suggested that lifetime predictions consider a representative set of deposition defects, as the most damaging defects arise from a complex combination of factors, such as the effective projected area and distance from the free surface. In this work, only the N largest defects for each specimen, based on the projected area, will be used to compute fatigue lifetime. This subset is considered representative of the deposition defects population, where N will be determined during model optimization. This approach is based on our previous research [96], where physics-informed neural networks were combined with the critical plane approach to predict the lifetime of LPBF-processed 316L stainless steel under multiaxial LCF loading. However, in this work, the model is reformulated for the LCF loading of LPBF-processed AlSi10Mg and significantly modified to accommodate a smaller input size, as only the results from eight LCF tests are available for AlSi10Mg.

The diagram of the proposed combined model is presented in Fig. 13. The ANN part features a single convolutional layer (CONV) and an output fully connected layer (FC). Based on the literature and testing, the following two defect parameters are used as network inputs: the Murakami parameter, \sqrt{area} , which is the square root of the projected area on the plane perpendicular to the loading [52, 45], and the shortest distance of the defect to the free surface, L . Given the limited dataset, the CONV layer is designed with

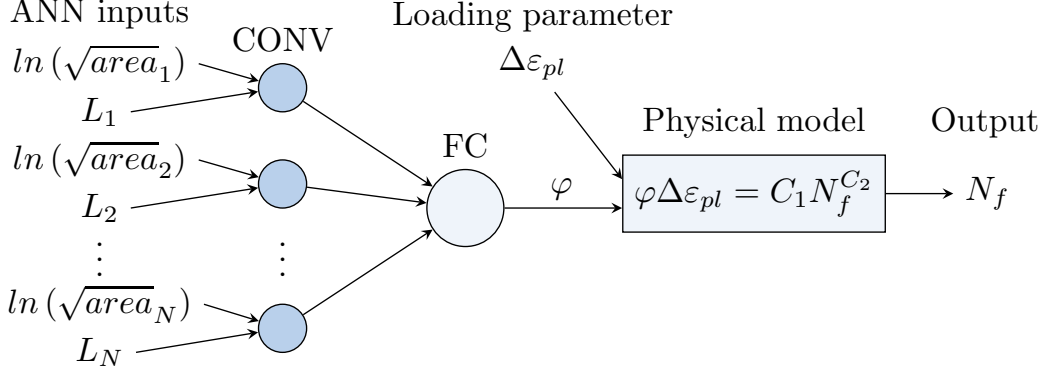


Figure 13: Diagram of the proposed combination of a physics-informed neural network with the strain-life approach.

one neuron in order to minimize the number of learnable parameters. The network has a single output, φ , which is produced by a single neuron in the FC layer. The network can be summarized by the following equations:

$$\varphi = y^{(2)} = g^{(2)}(z^{(2)}), \quad z^{(2)} = \sum_{i=1}^N w_i^{(2)} y_i^{(1)} + b^{(2)}, \quad (8)$$

$$y_i^{(1)} = g^{(1)}(z_i^{(1)}), \quad z_i^{(1)} = \sum_{k=1}^2 w_k^{(1)} x_k + b^{(1)}, \quad (9)$$

$${}^i\vec{x} = [\ln(\sqrt{area_i}), L_i]^T, \quad (10)$$

where ${}^i\vec{x}$ is the input vector consisting of the logarithm of the Murakami parameter and the shortest distance to the free surface of a defect with the index of i . The use of logarithm for the Murakami parameter will be explained later. The $\mathbf{w}^{(j)}$ are the weight matrices, $\vec{b}^{(j)}$ are the bias vectors, $\vec{y}^{(j)}$ are the output vectors of a layer, $g^{(j)}$ are the activation functions of the neurons, and the upper index j between brackets indicates the corresponding layer, i.e. 1, 2 indicate the CONV, FC layers, respectively.

The performance of the ANN can be enhanced by constraining the weights and biases, as well as making other modifications in order to align the model with known physical principles, resulting in a physics-informed neural network [68, 96]. In this setup, the output of the CONV layer, $y_i^{(1)}$, represents the contribution of each individual defect with index i to the overall damaging effect. The FC layer then combines these contributions into a damage-based parameter, φ , which characterizes the damaging effect of deposition defects. However, the model could easily become too focused on a single defect, which is undesirable. In order to handle each defect in the same way, the weights $w_i^{(2)}$ in Eq. 8 are set to be the same, i.e. $w_i^{(2)} = w^{(2)}$ for every i . This approach also significantly reduces the number of learnable parameters [96].

The next restrictions are derived from the properties of the derivatives and limits of φ with respect to the inputs. First, the properties of the derivatives with respect to the input are straightforward: the damaging effect increases with the size of the defect (described by \sqrt{area}) and decreases with the distance from the free surface [96]:

$$\frac{\partial \varphi}{\partial x_1} = \frac{\partial \varphi}{\partial \ln(\sqrt{area_i})} > 0, \quad \frac{\partial \varphi}{\partial x_2} = \frac{\partial \varphi}{\partial L_i} < 0. \quad (11)$$

The derivative with respect to the inputs is derived from Eq. 8 and 9 as follows:

$$\frac{\partial \varphi}{\partial x_k} = g^{(2)}(z^{(2)}) w^{(2)} g^{(1)}(z_i^{(1)}) w_k^{(1)}. \quad (12)$$

To satisfy the requirements in Eq. 11 for all possible inputs, it is evident that only monotonically increasing activation function can be utilized and the weights must meet the following: $w_1^{(1)} w^{(2)} > 0$ and $w_2^{(1)} w^{(2)} < 0$.

Similar statements apply to the limits of the correction parameter φ . For instance, since defects always have a damaging effect, the values of φ should range from between 1 and infinity, with $\varphi = 1$ indicating that the defects have no damaging effect:

$$\lim_{\forall i(\sqrt{area_i} \rightarrow 0)} \varphi = 1, \quad \lim_{\exists i(\sqrt{area_i} \rightarrow \infty)} \varphi = \infty, \quad \lim_{\forall i(L_i \rightarrow \infty)} \varphi = 1. \quad (13)$$

To implement these requirements, the output of the first layer, $y_i^{(1)}$, must be zero for defects with a zero projected size or defects that are infinitely distant from the free surface. Additionally, $y_i^{(1)}$ must approach infinity as the size of the defect increases. Therefore, the activation function for the CONV layer, $g^{(1)}$, is significantly restricted. It must approach zero as the argument approaches negative infinity, approach infinity as the argument approaches positive infinity, and be monotonically increasing. Among common activation functions, only the softplus function satisfies all three properties (Tab. 4) [96]. Finally, by using the logarithmic function for the Murakami parameter \sqrt{area} inputs and constraining the weights such that $w_1^{(1)} > 0$ and $w_2^{(1)} < 0$, the desired properties of $y_i^{(1)}$ are ensured. Combining these weight restrictions with the previously mentioned constraints, it follows that $w^{(2)} > 0$. With these constraints in place, the first and third limits in Eq. 13 are evaluated:

$$\lim_{\forall i(\sqrt{area_i} \rightarrow 0)} \varphi = \lim_{\forall i(L_i \rightarrow \infty)} \varphi = g^{(2)}(b^{(2)}). \quad (14)$$

For the regression problems, the identity function is commonly used for the output layer; therefore, $g^{(2)}(x) = x$ is chosen. Finally, by comparing Eq. 13 with Eq. 14, the final constraint emerges, $b^{(2)} = 1$.

Table 4: Softplus activation function.

Equation	Derivative	Output range
$g^{(2)}(x) = \ln(1 + e^x)$	$g^{(2)}(x) = \frac{1}{1+e^{-x}}$	$(0, \infty)$

Table 5: Weights and biases constraints.

Layer	Constraints
CONV	$w_{i1}^{(1)} > 0, \quad w_{i2}^{(1)} < 0$
FC	$w^{(2)} < 0, \quad b^{(2)} = 1$

To summarize, the logarithm function was used for the Murakami parameter inputs, the softmax activation function was selected for $g^{(1)}$, the identity function was chosen for

the output neuron $g^{(2)}$, and the weights and bias constraints given in Tab. 5 were designed to ensure that the network behaves according to known information in Eqs. 11 and 13.

Next, the parameters C_1 , C_2 , the weights and biases of the ANN have to be optimized to fit the experimental dataset. The dataset is divided into six data points for the training set and two data points for the testing set (one for the horizontal and one for the vertical build direction). The training set is used to optimize the parameters, while the testing set is used to verify that the model is not over-fitted and can generalize to new, unseen data points during optimization [96]. The model includes six real parameters and a single integer parameter N , which denotes the number of defects with the largest projected area used as inputs. The real parameters are optimized in Matlab using the Adam optimizer. Since the Adam optimizer has many parameters and no universal method for determining them, most were left at their default settings, with adjusted parameters shown in Tab. 6, chosen through trial and error. The loss function L was selected as the Mean Squared Error (MSE) of the logarithms of the numbers of cycles to failure. Weights and bias constraints (Tab. 5) are implemented by adding a penalization term to the loss function:

$$L = \sum_{i=1}^n (\ln(y_i) - \ln(t_i))^2 + f(w_1^{(1)}, w_2^{(1)}, w^{(2)}), \quad (15)$$

where y_i are the output values of the model, t_i are the observed fatigue lifetimes (targets), and f is a function that penalizes weight values not meeting the constraints in Tab. 5, and is otherwise zero.

Table 6: Parameters of the Adam optimizer.

No. epochs	Initial learning rate	Learning rate decay	Decay frequency
10^4	0.005	2%	50 epochs

To optimize the number of defects used as inputs, N , several values between 1 and 100 were tested, with the network trained for each value [96]. It should be noted that the most damaging defects are not known beforehand, as their impact depends on a combination of the Murakami parameter and the distance from the free surface. Therefore, the ANN is used not only to calculate φ , but also to determine how many defects with the largest projected area are necessary to adequately characterize the defect population within a specimen. Since the Adam optimizer is a local optimization method, the network was initialized and trained 200 times with random initial weights for each chosen N in order to maximize the chances of finding a local minimum close to the global minimum. The lowest MSE of the trained models is shown in Tab. 7, which indicates that the minimum MSE occurs near $N = 10$. Therefore, $N = 10$ was selected for further analysis.

Table 7: MSE of networks depending on number of input defects.

N	1	2	5	10	20	50	100
MSE	7.9×10^{-3}	4.5×10^{-3}	1.6×10^{-3}	5.7×10^{-4}	1.3×10^{-3}	3.3×10^{-3}	4×10^{-3}

A comparison of observed and predicted fatigue lifetimes is shown in Fig. 14. Model performance metrics, including the Mean Squared Error (MSE) and the coefficient of determination (R^2), are computed on a logarithmic scale across the entire experimental

dataset. A good correlation is achieved between the observed and predicted numbers of cycles to failure, as indicated by the coefficient of determination being close to 1. Additionally, the predictions for both the training and the two testing data points, which were not seen by the model during training, fall well within the two-times scatter band. This suggests that the model generalizes effectively within the range of the experimental dataset. In our previous research, we also utilized the sphericity of individual defects as an input for the ANN [96]. However, based on the obtained results, it appears that for AlSi10Mg the defect population could be appropriately described by a combination of the projected area and the distance of defects from the free surface of the specimens. Finally, it should be noted that the proposed ANN not only provided an expression for the damage parameter φ , but also determined the number of defects required to characterize the defect population within the specimens. In future work, the ANN-based models should be extended to predict the lifetime of complex components.

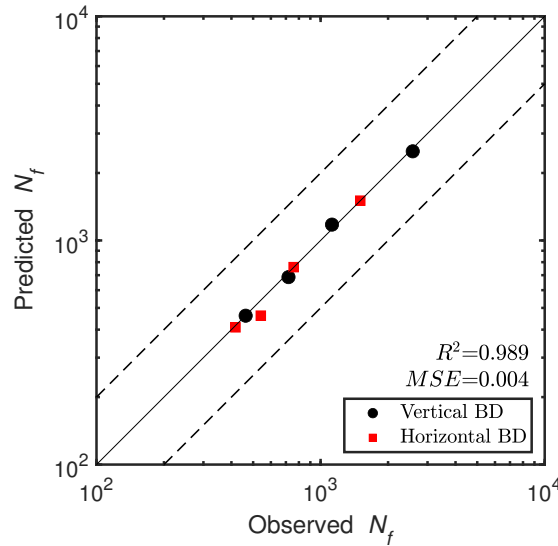


Figure 14: Prediction accuracy of the optimized model combining the strain-life approach with an ANN to account for the damaging effects of defects.

4. Conclusions

The mechanical behavior and microstructure of LPBF-processed AlSi10Mg aluminium alloy, which underwent 13 recycling cycles, were studied under LCF loading for vertically and horizontally built specimens. SEM and LM were employed to investigate damage mechanisms and microstructure, while X-ray CT was used to analyze the deposition defects. Subsequently, STEM was used to analyze deformation mechanisms at the nanoscale. This study quantified the effects of build direction and loading conditions on microstructure, damage, deformation mechanisms, fatigue lifetime, and stress-strain response. Additionally, a physics-informed neural network was proposed to correlate lifetime with loading and defect features. The findings presented in this study led to the following conclusions:

(1) The microstructure consisted of cells containing a supersaturated α -Al solid solution, separated by a continuous network of intercellular eutectic Si, for both virgin and recycled powder feedstocks. Additionally, Si-based precipitates occasionally appeared.

The use of recycled powder led to more pores in the microstructure, attributed to an increased oxygen content in the recycled powder compared to the virgin powder. On the other hand, size distribution curves were similar for both powder feedstocks. More LoF defects appeared in the horizontally built specimens due to their position on the build plate.

(2) The cyclic mechanical response stabilized after initial softening, with stress and plastic strain amplitudes being similar regardless of build direction. Horizontally built specimens exhibited a small tensile mean stress, while vertical ones showed a small compressive mean stress. Dislocation slip occurred mainly within cell interiors, as cell walls of eutectic Si and immobile dislocations restricted the movement of dislocations. The minor strength differences between build directions are explained by the Hall-Petch effect (due to eutectic cell walls), which is suggested as the main strengthening factor. Vertically built specimens, having larger effective cell sizes due to thermal gradients, provided a smaller mean free path for dislocations compared to horizontally built specimens.

(3) The fracture morphology exhibited predominant transgranular cracking and was similar for both vertical and horizontal build directions. Fatigue cracks initiated and propagated predominantly from LoF deposition defects close to the specimen surface. The fracture surfaces revealed various deposition defects such as defects resulting from the utilized deposition strategy, pores, and LoF. The fatigue cracks were occasionally, but not exclusively, found to follow the melt pool boundaries, with a greater frequency of occurrence for vertically built specimens.

(4) The lifetime under LCF loading was more influenced by the number of LoF deposition defects than by the build direction. Horizontally built specimens had a lower fatigue lifetime compared to vertically built ones, especially at lower strain amplitudes; at the highest strain amplitude, the lifetimes were similar. This was due to more LoF defects in the horizontally built specimens acting as stress concentrators. It is concluded that the position of specimens on the build plate, with respect to the number of deposition defects, impacts the resulting microstructure more than the use of powder recycled for 13 cycles.

(5) A good correlation between the experimental and numerical results for fatigue lifetime was observed for LPBF-processed AlSi10Mg using the proposed physics-informed neural network-based damage model. The model coupled an ANN with the strain-life approach represented by the Manson-Coffin law. The utilization of the ANN allowed for the determination of a damage parameter that characterizes the effect of deposition defects on fatigue lifetime. It was demonstrated that machine learning can be effectively utilized, even with a small dataset. In future work, the ANN-based models will be extended to predict the lifetimes of more complex components.

CRedit author statement

Michal Bartošák: Writing – original draft, Writing – review & editing, Investigation, Supervision, Methodology, Conceptualization, Data visualization, Data curation. **Michal Jambor:** Writing – original draft, Writing – review & editing, Investigation, Methodology, Data visualization. **Jiří Halamka:** Writing – original draft, Investigation, Software. **Lukáš Pelikán:** Writing – original draft, Resources, Methodology. **Ondřej Stránský:** Methodology, Investigation, Data visualization. **Eliška Galčíková:** Methodology, Investigation, Data visualization. **Jakub Horváth:** Investigation, Data visualization. **Michal Slaný:** Investigation. **Šimon Petrášek:** Investigation. **Ivo Šulák:** Writing – original draft, Writing – review & editing, Investigation, Methodology.

Data availability

Data of this study can be accessed in Zenodo (DOI: 10.5281/zenodo.13828238).

Acknowledgement

Michal Bartošák, Ondřej Stránský, Eliška Galčíková, Michal Slaný, Jakub Horváth, Lukáš Pelikán and Šimon Petrášek acknowledge support from the Future Fund of Czech Technical University in Prague. Michal Jambor and Ivo Šulák acknowledge the support from the project "Mechanical Engineering of Biological and Bio-inspired Systems", funded as project No. CZ.02.01.01/00/22_008/0004634 by Programme Johannes Amos Comenius, call Excellent Research.

References

- [1] A. Simchi, Direct laser sintering of metal powders: Mechanism, kinetics and microstructural features, *Materials Science and Engineering: A* 428 (1-2) (2006) 148–158.
- [2] J. H. Martin, B. D. Yahata, J. M. Hundley, J. A. Mayer, T. A. Schaedler, T. M. Pollock, 3d printing of high-strength aluminium alloys, *Nature* 549 (7672) (2017) 365–369.
- [3] D. Herzog, V. Seyda, E. Wycisk, C. Emmelmann, Additive manufacturing of metals, *Acta Materialia* 117 (2016) 371–392.
- [4] W. E. Frazier, Metal additive manufacturing: a review, *Journal of Materials Engineering and performance* 23 (2014) 1917–1928.
- [5] D. D. Gu, W. Meiners, K. Wissenbach, R. Poprawe, Laser additive manufacturing of metallic components: materials, processes and mechanisms, *International materials reviews* 57 (3) (2012) 133–164.
- [6] L. E. Murr, S. M. Gaytan, D. A. Ramirez, E. Martinez, J. Hernandez, K. N. Amato, P. W. Shindo, F. R. Medina, R. B. Wicker, Metal fabrication by additive manufacturing using laser and electron beam melting technologies, *Journal of Materials Science & Technology* 28 (1) (2012) 1–14.
- [7] X. Li, X. Wang, M. Saunders, A. Suvorova, L. Zhang, Y. Liu, M. Fang, Z. Huang, T. B. Sercombe, A selective laser melting and solution heat treatment refined al–12si alloy with a controllable ultrafine eutectic microstructure and 25% tensile ductility, *Acta Materialia* 95 (2015) 74–82.
- [8] L. Thijs, K. Kempen, J.-P. Kruth, J. Van Humbeeck, Fine-structured aluminium products with controllable texture by selective laser melting of pre-alloyed alsi10mg powder, *Acta Materialia* 61 (5) (2013) 1809–1819.
- [9] X. P. Li, G. Ji, Z. Chen, A. Addad, Y. Wu, H. Wang, J. Vleugels, J. Van Humbeeck, J.-P. Kruth, Selective laser melting of nano-tib2 decorated alsi10mg alloy with high fracture strength and ductility, *Acta Materialia* 129 (2017) 183–193.

- [10] C. Y. Yap, C. K. Chua, Z. L. Dong, Z. H. Liu, D. Q. Zhang, L. E. Loh, S. L. Sing, Review of selective laser melting: Materials and applications, *Applied physics reviews* 2 (4).
- [11] H. Tang, M. Qian, N. Liu, X. Zhang, G. Yang, J. Wang, Effect of powder reuse times on additive manufacturing of ti-6al-4v by selective electron beam melting, *Jom* 67 (3) (2015) 555–563.
- [12] A. H. Maamoun, M. Elbestawi, G. K. Dosbaeva, S. C. Veldhuis, Thermal post-processing of alsil0mg parts produced by selective laser melting using recycled powder, *Additive Manufacturing* 21 (2018) 234–247.
- [13] M. Rafieazad, A. Chatterjee, A. Nasiri, Effects of recycled powder on solidification defects, microstructure, and corrosion properties of dmls fabricated alsil0mg, *Jom* 71 (2019) 3241–3252.
- [14] A. Hadadzadeh, C. Baxter, B. S. Amirkhiz, M. Mohammadi, Strengthening mechanisms in direct metal laser sintered alsil0mg: Comparison between virgin and recycled powders, *Additive Manufacturing* 23 (2018) 108–120.
- [15] M. Coşkun, K. C. Dizdar, G. Tarakçı, G. Özer, D. Dispınar, Recycling of additive manufactured alsil0mg and its effect on mechanical properties, *Materials Chemistry and Physics* 289 (2022) 126411.
- [16] E. Brandl, U. Heckenberger, V. Holzinger, D. Buchbinder, Additive manufactured alsil0mg samples using selective laser melting (slm): Microstructure, high cycle fatigue, and fracture behavior, *Materials & Design* 34 (2012) 159–169.
- [17] N. Read, W. Wang, K. Essa, M. M. Attallah, Selective laser melting of alsil0mg alloy: Process optimisation and mechanical properties development, *Materials & Design* (1980-2015) 65 (2015) 417–424.
- [18] W. Li, S. Li, J. Liu, A. Zhang, Y. Zhou, Q. Wei, C. Yan, Y. Shi, Effect of heat treatment on alsil0mg alloy fabricated by selective laser melting: Microstructure evolution, mechanical properties and fracture mechanism, *Materials Science and Engineering: A* 663 (2016) 116–125.
- [19] P. Fathi, M. Mohammadi, X. Duan, A. M. Nasiri, A comparative study on corrosion and microstructure of direct metal laser sintered alsil0mg_200c and die cast a360. 1 aluminum, *Journal of Materials Processing Technology* 259 (2018) 1–14.
- [20] P. Delroisse, P. J. Jacques, E. Maire, O. Rigo, A. Simar, Effect of strut orientation on the microstructure heterogeneities in alsil0mg lattices processed by selective laser melting, *Scripta Materialia* 141 (2017) 32–35.
- [21] A. Hadadzadeh, B. S. Amirkhiz, J. Li, A. Odeshi, M. Mohammadi, Deformation mechanism during dynamic loading of an additively manufactured alsil0mg_200c, *Materials Science and Engineering: A* 722 (2018) 263–268.
- [22] M. J. Paul, Q. Liu, J. P. Best, X. Li, J. J. Kruzic, U. Ramamurty, B. Gludovatz, Fracture resistance of alsil0mg fabricated by laser powder bed fusion, *Acta Materialia* 211 (2021) 116869.

- [23] Y. Zheng, Z. Zhao, R. Xiong, G. Ren, M. Yao, W. Liu, L. Zang, Effect of post heat treatment on microstructure, mechanical property and corrosion behavior of alsil0mg alloy fabricated by selective laser melting, *Progress in Natural Science: Materials International* 34 (1) (2024) 89–101.
- [24] E. Maleki, N. Shamsaei, A comprehensive study on the effects of surface post-processing on fatigue performance of additively manufactured alsil0mg: An augmented machine learning perspective on experimental observations, *Additive Manufacturing* 86 (2024) 104179.
- [25] Z. Wu, S. Wu, J. Bao, W. Qian, S. Karabal, W. Sun, P. J. Withers, The effect of defect population on the anisotropic fatigue resistance of alsil0mg alloy fabricated by laser powder bed fusion, *International Journal of Fatigue* 151 (2021) 106317.
- [26] B. Chen, S. Moon, X. Yao, G. Bi, J. Shen, J. Umeda, K. Kondoh, Strength and strain hardening of a selective laser melted alsil0mg alloy, *Scripta Materialia* 141 (2017) 45–49.
- [27] E. Zaretsky, A. Stern, N. Frage, Dynamic response of alsil0mg alloy fabricated by selective laser melting, *Materials Science and Engineering: A* 688 (2017) 364–370.
- [28] J. Wu, X. Wang, W. Wang, M. Attallah, M. Loretto, Microstructure and strength of selectively laser melted alsil0mg, *Acta Materialia* 117 (2016) 311–320.
- [29] A. Hadadzadeh, B. S. Amirkhiz, A. Odeshi, J. Li, M. Mohammadi, Role of hierarchical microstructure of additively manufactured alsil0mg on dynamic loading behavior, *Additive Manufacturing* 28 (2019) 1–13.
- [30] R. Chou, A. Ghosh, S. Chou, M. Paliwal, M. Brochu, Microstructure and mechanical properties of al10sing fabricated by pulsed laser powder bed fusion, *Materials Science and Engineering: A* 689 (2017) 53–62.
- [31] K. G. Prashanth, S. Scudino, H. J. Klauss, K. B. Surreddi, L. Löber, Z. Wang, A. K. Chaubey, U. Kühn, J. Eckert, Microstructure and mechanical properties of al–12si produced by selective laser melting: Effect of heat treatment, *Materials Science and Engineering: A* 590 (2014) 153–160.
- [32] A. Leicht, U. Klement, E. Hryha, Effect of build geometry on the microstructural development of 316l parts produced by additive manufacturing, *Materials Characterization* 143 (2018) 137–143.
- [33] J. Pegues, M. Roach, R. S. Williamson, N. Shamsaei, Surface roughness effects on the fatigue strength of additively manufactured ti-6al-4v, *International Journal of Fatigue* 116 (2018) 543–552.
- [34] A. Du Plessis, S. Beretta, Killer notches: The effect of as-built surface roughness on fatigue failure in alsil0mg produced by laser powder bed fusion, *Additive Manufacturing* 35 (2020) 101424.
- [35] N. Sanaei, A. Fatemi, Defects in additive manufactured metals and their effect on fatigue performance: A state-of-the-art review, *Progress in Materials Science* 117 (2021) 100724.

- [36] P. Foti, N. Razavi, A. Fatemi, F. Berto, Multiaxial fatigue of additively manufactured metallic components: A review of the failure mechanisms and fatigue life prediction methodologies, *Progress in Materials Science* 137 (2023) 101126.
- [37] N. E. Uzan, R. Shneck, O. Yeheskel, N. Frage, Fatigue of alsil0mg specimens fabricated by additive manufacturing selective laser melting (am-slm), *Materials Science and Engineering: A* 704 (2017) 229–237.
- [38] J. P. Isaac, S. Lee, S. Thompson, A. Saharan, N. Shamsaei, H. V. Tippur, Role of build orientation on quasi-static and dynamic fracture responses of additively manufactured al357 and alsil0mg alloys, *Additive Manufacturing* 59 (2022) 103080.
- [39] K. S. Stopka, M. D. Sangid, Modeling fatigue behavior of additively manufactured alloys with an emphasis on pore defect morphology, *Journal of the Mechanics and Physics of Solids* 181 (2023) 105429.
- [40] P. Ferro, A. Fabrizi, F. Berto, G. Savio, R. Meneghello, S. Rosso, Defects as a root cause of fatigue weakening of additively manufactured alsil0mg components, *Theoretical and Applied Fracture Mechanics* 108 (2020) 102611.
- [41] T. D. Piette, R. J. Warren, A. G. Spangenberg, E. J. Hummelt, D. A. Lados, Microstructure evolution, fatigue crack growth, and ultrasonic fatigue in as-fabricated laser powder bed and conventionally cast al–10si-0.4 mg: A mechanistic understanding and integrated flaw-sensitive fatigue design methods, *Materials Science and Engineering: A* 825 (2021) 141892.
- [42] S. Romano, L. Patriarca, S. Foletti, S. Beretta, Lcf behaviour and a comprehensive life prediction model for alsil0mg obtained by slm, *International Journal of fatigue* 117 (2018) 47–62.
- [43] Y. Nadot, C. Nadot-Martin, W. H. Kan, S. Boufadene, M. Foley, J. Cairney, G. Proust, L. Ridosz, Predicting the fatigue life of an alsil0mg alloy manufactured via laser powder bed fusion by using data from computed tomography, *Additive Manufacturing* 32 (2020) 100899.
- [44] G. Qian, Z. Jian, Y. Qian, X. Pan, X. Ma, Y. Hong, Very-high-cycle fatigue behavior of alsil0mg manufactured by selective laser melting: Effect of build orientation and mean stress, *International Journal of Fatigue* 138 (2020) 105696.
- [45] Y. Murakami, *Metal fatigue: effects of small defects and nonmetallic inclusions*, Academic Press, 2019.
- [46] C. Fischer, C. Schweizer, Lifetime assessment of the process-dependent material properties of additive manufactured alsil0mg under low-cycle fatigue loading, in: *MATEC Web of Conferences*, Vol. 326, EDP Sciences, 2020, p. 07003.
- [47] Z. Xu, A. Liu, X. Wang, Fatigue performance and crack propagation behavior of selective laser melted alsil0mg in 0, 15, 45 and 90 building directions, *Materials Science and Engineering: A* 812 (2021) 141141.
- [48] W. Qian, S. Wu, Z. Wu, S. Ahmed, W. Zhang, G. Qian, P. J. Withers, In situ x-ray imaging of fatigue crack growth from multiple defects in additively manufactured alsil0mg alloy, *International Journal of Fatigue* 155 (2022) 106616.

- [49] F. Del Re, V. Contaldi, A. Astarita, B. Palumbo, A. Squillace, P. Corrado, P. Di Petta, Statistical approach for assessing the effect of powder reuse on the final quality of alsi10mg parts produced by laser powder bed fusion additive manufacturing, *The International Journal of Advanced Manufacturing Technology* 97 (2018) 2231–2240.
- [50] H. Asgari, C. Baxter, K. Hosseinkhani, M. Mohammadi, On microstructure and mechanical properties of additively manufactured alsi10mg_200c using recycled powder, *Materials Science and Engineering: A* 707 (2017) 148–158.
- [51] F. Sausto, P. Carrion, N. Shamsaei, S. Beretta, Fatigue failure mechanisms for alsi10mg manufactured by l-pbf under axial and torsional loads: The role of defects and residual stresses, *International Journal of Fatigue* 162 (2022) 106903.
- [52] Y. Murakami, S. Beretta, Small defects and inhomogeneities in fatigue strength: experiments, models and statistical implications, *Extremes* 2 (1999) 123–147.
- [53] N. Sanaei, A. Fatemi, Analysis of the effect of internal defects on fatigue performance of additive manufactured metals, *Materials Science and Engineering: A* 785 (2020) 139385.
- [54] S. Beretta, S. Romano, A comparison of fatigue strength sensitivity to defects for materials manufactured by am or traditional processes, *International Journal of Fatigue* 94 (2017) 178–191.
- [55] R. Molaei, A. Fatemi, N. Sanaei, J. Pegues, N. Shamsaei, S. Shao, P. Li, D. Warner, N. Phan, Fatigue of additive manufactured ti-6al-4v, part ii: The relationship between microstructure, material cyclic properties, and component performance, *International Journal of Fatigue* 132 (2020) 105363.
- [56] X. Niu, C. He, S.-P. Zhu, P. Foti, F. Berto, L. Wang, D. Liao, Q. Wang, Defect sensitivity and fatigue design: Deterministic and probabilistic aspects in am metallic materials, *Progress in Materials Science* (2024) 101290.
- [57] V. Prithivirajan, M. D. Sangid, The role of defects and critical pore size analysis in the fatigue response of additively manufactured in718 via crystal plasticity, *Materials & Design* 150 (2018) 139–153.
- [58] R. Biswal, A. K. Syed, X. Zhang, Assessment of the effect of isolated porosity defects on the fatigue performance of additive manufactured titanium alloy, *Additive Manufacturing* 23 (2018) 433–442.
- [59] Y. Wang, Z. Su, Effect of micro-defects on fatigue lifetime of additive manufactured 316l stainless steel under multiaxial loading, *Theoretical and Applied Fracture Mechanics* 111 (2021) 102849.
- [60] L. Afroz, S. Inverarity, M. Qian, M. Easton, R. Das, Analysing the effect of defects on stress concentration and fatigue life of l-pbf alsi10mg alloy using finite element modelling, *Progress in Additive Manufacturing* 9 (2) (2024) 341–359.
- [61] H. Bao, S. Wu, Z. Wu, G. Kang, X. Peng, P. J. Withers, A machine-learning fatigue life prediction approach of additively manufactured metals, *Engineering Fracture Mechanics* 242 (2021) 107508.

- [62] M. Bartošák, Using machine learning to predict lifetime under isothermal low-cycle fatigue and thermo-mechanical fatigue loading, *International Journal of Fatigue* (2022) 107067.
- [63] J. F. Barbosa, J. A. Correia, R. F. Júnior, A. M. De Jesus, Fatigue life prediction of metallic materials considering mean stress effects by means of an artificial neural network, *International Journal of fatigue* 135 (2020) 105527.
- [64] X.-C. Zhang, J.-G. Gong, F.-Z. Xuan, A deep learning based life prediction method for components under creep, fatigue and creep-fatigue conditions, *International Journal of Fatigue* 148 (2021) 106236.
- [65] J. Yang, G. Kang, Q. Kan, A novel deep learning approach of multiaxial fatigue life-prediction with a self-attention mechanism characterizing the effects of loading history and varying temperature, *International Journal of Fatigue* 162 (2022) 106851.
- [66] J. Li, Z. Yang, G. Qian, F. Berto, Machine learning based very-high-cycle fatigue life prediction of ti-6al-4v alloy fabricated by selective laser melting, *International Journal of Fatigue* 158 (2022) 106764.
- [67] Z. Zhan, H. Li, Machine learning based fatigue life prediction with effects of additive manufacturing process parameters for printed ss 316l, *International Journal of Fatigue* 142 (2021) 105941.
- [68] J. Halamka, M. Bartošák, M. Španiel, Using hybrid physics-informed neural networks to predict lifetime under multiaxial fatigue loading, *Engineering Fracture Mechanics* 289 (2023) 109351.
- [69] D. Chen, Y. Li, K. Liu, Y. Li, A physics-informed neural network approach to fatigue life prediction using small quantity of samples, *International Journal of Fatigue* 166 (2023) 107270.
- [70] M. Raissi, P. Perdikaris, G. E. Karniadakis, Physics-informed neural networks: A deep learning framework for solving forward and inverse problems involving nonlinear partial differential equations, *Journal of Computational physics* 378 (2019) 686–707.
- [71] X.-C. Zhang, J.-G. Gong, F.-Z. Xuan, A physics-informed neural network for creep-fatigue life prediction of components at elevated temperatures, *Engineering Fracture Mechanics* 258 (2021) 108130.
- [72] E. Salvati, A. Tognan, L. Laurenti, M. Pelegatti, F. De Bona, A defect-based physics-informed machine learning framework for fatigue finite life prediction in additive manufacturing, *Materials & Design* 222 (2022) 111089.
- [73] L. Wang, S.-P. Zhu, C. Luo, D. Liao, Q. Wang, Physics-guided machine learning frameworks for fatigue life prediction of am materials, *International Journal of Fatigue* 172 (2023) 107658.
- [74] M. Bartošák, M. Nagode, J. Klemenc, K. Doubrava, D. Šeruga, Use of Prandtl operators in simulating the cyclic softening of Inconel 718 under isothermal low-cycle fatigue loading, *International Journal of Mechanical Sciences* 222 (2022) 107182.

- [75] M. Bartošák, I. Šulák, J. Horváth, M. Jambor, L. Pilsová, Isothermal low-cycle fatigue and fatigue-creep behaviour of 2618 aluminium alloy, *International Journal of Fatigue* (2023) 108027.
- [76] M. Bartošák, J. Horváth, Isothermal low-cycle fatigue, fatigue-creep and thermo-mechanical fatigue of SiMo 4.06 cast iron: Damage mechanisms and life prediction, *Engineering Fracture Mechanics* 288 (2023) 109316.
- [77] T. Marrow, I. Šulák, B.-S. Li, M. Vukšić, M. Williamson, D. Armstrong, High temperature spherical nano-indentation of graphite crystals, *Carbon* 191 (2022) 236–242.
- [78] D. Powell, A. E. Rennie, L. Geekie, N. Burns, Understanding powder degradation in metal additive manufacturing to allow the upcycling of recycled powders, *Journal of Cleaner Production* 268 (2020) 122077.
- [79] V. V. Popov Jr, A. Katz-Demyanetz, A. Garkun, M. Bamberger, The effect of powder recycling on the mechanical properties and microstructure of electron beam melted ti-6al-4 v specimens, *Additive Manufacturing* 22 (2018) 834–843.
- [80] C. L. A. Leung, S. Marussi, M. Towrie, R. C. Atwood, P. J. Withers, P. D. Lee, The effect of powder oxidation on defect formation in laser additive manufacturing, *Acta Materialia* 166 (2019) 294–305.
- [81] J. H. Tan, W. L. E. Wong, K. W. Dalgarno, An overview of powder granulometry on feedstock and part performance in the selective laser melting process, *Additive Manufacturing* 18 (2017) 228–255.
- [82] R. Hague, S. Mansour, N. Saleh, Material and design considerations for rapid manufacturing, *International Journal of Production Research* 42 (22) (2004) 4691–4708.
- [83] S. A. Khairallah, A. A. Martin, J. R. Lee, G. Guss, N. P. Calta, J. A. Hammons, M. H. Nielsen, K. Chaput, E. Schwalbach, M. N. Shah, et al., Controlling interdependent meso-nanosecond dynamics and defect generation in metal 3d printing, *Science* 368 (6491) (2020) 660–665.
- [84] M. Fousová, D. Dvorský, A. Michalcová, D. Vojtěch, Changes in the microstructure and mechanical properties of additively manufactured alsi10mg alloy after exposure to elevated temperatures, *Materials Characterization* 137 (2018) 119–126.
- [85] J. Zhao, B. Li, G. Chen, T. Itoh, X. Chen, Effects of dwell time on the isothermal and thermomechanical fatigue behavior of 316ln stainless steel, *International Journal of Fatigue* 162 (2022) 106989.
- [86] S. Romano, A. Brückner-Foit, A. Brandão, J. Gumpinger, T. Ghidini, S. Beretta, Fatigue properties of alsi10mg obtained by additive manufacturing: Defect-based modelling and prediction of fatigue strength, *Engineering Fracture Mechanics* 187 (2018) 165–189.
- [87] Y. Chen, X. Wang, Y. Peng, Y. Jiang, X. Yang, S. B. Leen, J. Gong, et al., Deformation mechanisms of selective laser melted 316l austenitic stainless steel in high temperature low cycle fatigue, *Materials Science and Engineering: A* 843 (2022) 143123.

- [88] C.-H. Yu, A. Leicht, R. L. Peng, J. Moverare, Low cycle fatigue of additively manufactured thin-walled stainless steel 316l, *Materials Science and Engineering: A* 821 (2021) 141598.
- [89] S. R. Ch, A. Raja, P. Nadig, R. Jayaganthan, N. Vasa, Influence of working environment and built orientation on the tensile properties of selective laser melted als10mg alloy, *Materials Science and Engineering: A* 750 (2019) 141–151.
- [90] A. N. R. Rajan, M. Krochmal, M. Shahmardani, T. Wegener, A. Hartmaier, T. Nien-dorf, G. Moeini, Micromechanical modeling of the low-cycle fatigue behavior of ad-ditively manufactured als10mg, *Materials Science and Engineering: A* 879 (2023) 145232.
- [91] C. Cai, H. Geng, Z. Zhang, Temperature-dependent cyclic response and microstruc-ture of als10mg (cu) alloy, *Materials Characterization* 141 (2018) 148–155.
- [92] B. OH, The exponential law of endurance tests, in: *Proc Am Soc Test Mater*, Vol. 10, 1910, pp. 625–630.
- [93] L. F. Coffin Jr, A study of the effects of cyclic thermal stresses on a ductile metal, *Transactions of the American Society of Mechanical Engineers*, New York 76 (1954) 931–950.
- [94] S. S. Manson, Behavior of materials under conditions of thermal stress, Vol. 2933, National Advisory Committee for Aeronautics, 1953.
- [95] W. Ramberg, W. Osgood, Description of stress-strain curves by three parameters. naca, tech, No902.
- [96] M. Bartošák, J. Halamka, L. Beránek, M. Koukolíková, M. Slaný, M. Pagáč, J. Džugan, Using physics-informed neural networks to predict the lifetime of laser powder bed fusion processed 316l stainless steel under multiaxial low-cycle fatigue loading, *International Journal of Fatigue* (2024) 108608.